

RANS Modelling in Transonic S-Ducts with Passive Flow Control

Journal:	<i>Part A: Journal of Power and Energy</i>
Manuscript ID	JPE-18-0344.R1
Manuscript Type:	Original Article
Date Submitted by the Author:	06-Mar-2019
Complete List of Authors:	Hickling, Tom; University of Oxford, Department of Engineering Science Ingram, Grant; Durham University, Department of Engineering
Keywords:	CFD, S-duct, RANS, Tubercles
Abstract:	<p>S-duct diffusers are used in aircraft with embedded engines to route ambient air to the fan face. Sizing and stealth considerations drive a need for high curvature ducts, but the curvature causes complex secondary flows that lead to total pressure distortion and swirl velocities at the engine face. These must be controlled for stable engine operation. In this paper, tubercles, a novel bio-inspired passive flow control method, are analysed numerically in a duct with transonic flow. The results are compared to experimental data obtained as part of a campaign at the Royal Military College, Canada to investigate the effects of S-duct geometry and novel passive flow control devices on the performance of transonic S-ducts. The performance of RANS turbulence models in the S-ducts is assessed - Menter's SST model predicts excessive losses due to the over-activity of its stress limiter. The realisable k-ϵ model gives a significant improvement in the prediction of static pressure distributions, but losses and distortion characteristics are predicted poorly due to the model's inability to resolve the effects of unsteadiness in separated regions. Large tubercle geometries are found to trigger earlier separation in the centre of the duct by concentrating low momentum fluid in valleys, but they also act as boundary layer fences away from the duct centre. Smaller geometries are found to generate vortices that re-energise the boundary layer, delaying flow separation. Methods are recommended for future computational analyses of S-ducts and new designs of tubercles.</p>

1
2
3
4
5
6
7
8
9
10
11
12
13
14
15
16
17
18
19
20
21
22
23
24
25
26
27
28
29
30
31
32
33
34
35
36
37
38
39
40
41
42
43
44
45
46
47
48
49
50
51
52
53
54
55
56
57
58
59
60

Note: The following files were submitted by the author for peer review, but cannot be converted to PDF. You must view these files (e.g. movies) online.

JPE-18-0344.R1_clean_files_2.zip



RANS Modelling in Transonic S-Ducts with Passive Flow Control

Journal Title
 XX(X):1-14
 ©The Author(s) 0000
 Reprints and permission:
 sagepub.co.uk/journalsPermissions.nav
 DOI: 10.1177/ToBeAssigned
 www.sagepub.com/

SAGE

Tom Hickling^{1, 2} and Grant Ingram¹

Abstract

S-duct diffusers are used in aircraft with embedded engines to route ambient air to the fan face. Sizing and stealth considerations drive a need for high curvature ducts, but the curvature causes complex secondary flows that lead to total pressure distortion and swirl velocities at the engine face. These must be controlled for stable engine operation. In this paper, tubercles, a novel bio-inspired passive flow control method, are analysed numerically in a duct with transonic flow. The results are compared to experimental data obtained as part of a campaign at the Royal Military College, Canada to investigate the effects of S-duct geometry and novel passive flow control devices on the performance of transonic S-ducts. The performance of RANS turbulence models in the S-ducts is assessed - Menter's SST model predicts excessive losses due to the over-activity of its stress limiter. The realisable $k-\epsilon$ model gives a significant improvement in the prediction of static pressure distributions, but losses and distortion characteristics are predicted poorly due to the model's inability to resolve the effects of unsteadiness in separated regions. Large tubercle geometries are found to trigger earlier separation in the centre of the duct by concentrating low momentum fluid in valleys, but they also act as boundary layer fences away from the duct centre. Smaller geometries are found to generate vortices that re-energise the boundary layer, delaying flow separation. Methods are recommended for future computational analyses of S-ducts and new designs of tubercles.

Keywords

CFD, S-duct, RANS, Tubercles

Introduction

This report discusses the use of computational fluid dynamics (CFD) to lend insight to experimental data on tubercles (a novel flow control device) in transitioning S-duct diffusers by Asghar et al. at the Royal Military College (RMC), Canada¹. Following an overview of the S-ducts and performance measures considered, this paper presents the computational methodology and five sections of results: an investigation of the performance of RANS turbulence models in the ducts; discussions of the static pressure, swirl, and total pressure distributions; and a more detailed analysis of the effects of tubercles on the flow field. Finally, suitable methods are recommended for future computations on S-ducts with passive flow control.

One of the ducts analysed is shown in Fig. 1, with the tubercle locations on the inside of both bends highlighted. The profiles and key dimensions (amplitude, A , and wavelength, λ) of the three tubercle geometries are given in Fig 2. The experimental data used for validation of the CFD results consisted of steady wall static pressure measurements on the top and bottom meridian of the ducts, and steady total pressure measurements at the duct exits. 3D effects such as swirl and the topology of separated regions can not be investigated using the experimental data, leading to a need for CFD flow fields to enable the flow mechanisms behind the experimental results to be investigated. The CFD flow fields can be used to complement the existing

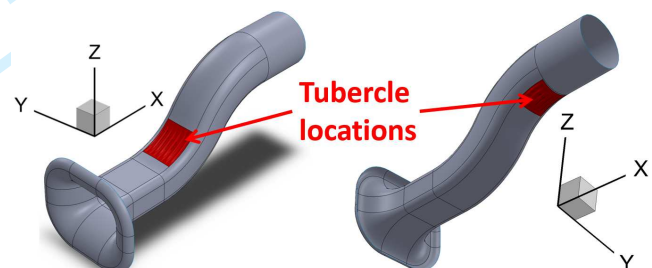


Figure 1. Isometric view of the RMC S-duct. Left: From above. Right: From below.

design philosophy, allowing for more informed decisions to be made when improving the tubercles.

The function of an S-duct diffuser is to redirect flow from the outside of the fuselage of an air vehicle and decelerate it before the fan face of an embedded engine². An engine face Mach number of 0.4-0.6 is usually targeted³. S-ducts are often used in unmanned aerial vehicles (UAVs), older transport aircraft, combat aircraft, cruise missiles^{3,4}, and boundary layer ingesting propulsion on blended wing/body designs⁵. To avoid a degradation in compressor surge margin and propulsion system efficiency, an ideal S-duct would provide a

¹Department of Engineering, Durham University.

²Currently Department of Engineering Science, University of Oxford.

Corresponding author:

Tom Hickling

Email: tom.hickling@eng.ox.ac.uk

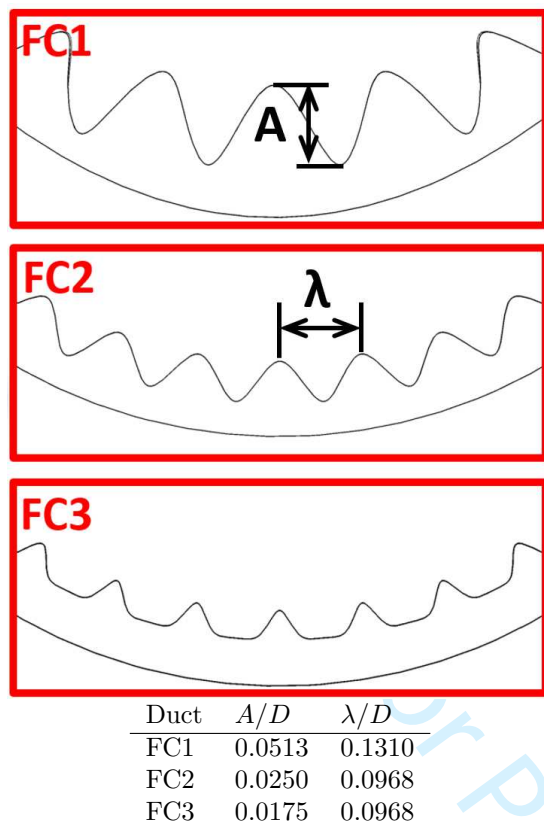


Figure 2. Tubercle dimensions. D is the diameter of the duct outlet, 0.1016 m.

uniform axial velocity and pressure distribution at the engine face², but the behaviour of the boundary layer in the hostile environment of an adverse pressure gradient and duct curvature causes secondary flows and separations which complicate intake development. Due to this, large S-duct curvatures are avoided where possible⁶.

However, there are many motivations for the use of high offset/curvature S-ducts. The first of these is space constraints and weight savings. For instance the McDonnell Douglas F/A-18 Hornet is a small aircraft, it thus requires short, highly curved S-ducts to route the air from outside the fuselage to its twin embedded engines². Current UAVs are another case in point, as the length of the propulsion system is currently dictating the overall size of the aircraft⁶. High curvature ducts are also useful for the reduction of an aircraft's Radar Cross Section (RCS) - low RCS intake design necessitates 100% line-of-sight blockage of the engine fan rotor⁷. Examples of this on combat aircraft are the Lockheed-Martin F-22 Raptor and F-35 Lightning II. Due to the advantages of high offset S-ducts, there is considerable interest in using flow control devices to control the secondary flows and separation within the duct, alleviating the negative effects of the adverse pressure gradient and duct curvature.

S-duct flows

Intrinsic S-duct flow regime

The intrinsic flow mechanism in S-duct diffusers is well known, and often given in textbooks on internal flow and intake aerodynamics. In the first bend, the centrifugal pressure gradient is proportional to $\rho U^2/R$, where U is the free stream velocity, ρ is the fluid density, and R is the duct radius of curvature. Considering now the low-momentum fluid in the boundary layer, moving with velocity $U' < U$, the local pressure gradient $\rho U'^2/R$ is too small to balance the pressure difference between the inside and outside of the bend, leading to the boundary layer fluid migrating to the inside of the bend, and the high velocity core migrating to the outside⁸. If the boundary layer at the inlet is symmetrical, the flow will return to the outside of the bend across the middle of the duct⁹, rolling up into two discrete contra-rotating vortical structures called Dean vortices¹⁰.

In the second bend, the centrifugal pressure gradient is reversed in direction, and the low momentum fluid (inside of the first bend), where it is not in a position to be driven back circumferentially - it thus persists to the engine face face⁹. Viscous effects provide the initial low momentum fluid that causes the secondary flow, but the generation and downstream evolution of the vortices is predominantly an inviscid effect¹⁰. In diffusers with sharp bends, wall static pressure measurements have implied the existence of a separated region caused by the interaction of the adverse pressure gradient and migrated low-momentum fluid existed downstream of the first bend. This was confirmed by laser doppler anemometry measurements performed by Whitelaw and Yu⁸. Due to the presence of several interacting flow mechanisms, turbulent S-duct flows are very challenging to predict accurately¹¹.

S-duct performance

Widely used reduced order metrics for quantitatively assessing the three aspects of S-duct steady state performance are outlined below, definitions are given in the appendix. The coefficients are considered on the Aerodynamic Interface Plane (AIP), the location of which is generally agreed upon by engine and airframe manufacturers.

Total pressure loss: High values of total pressure loss within the intake lead to a reduction in the overall efficiency of the propulsion system¹², and are also often symptomatic of issues with total pressure distortion and swirl. It is measured by the average total pressure loss coefficient,

$$\gamma_{avg} = 1 - (p_{02}/p_{01}) = 1 - \pi_{avg} \quad (1)$$

where p_{02} and p_{01} are the average total pressure on the AIP and inlet, and π_{avg} is the average total pressure ratio.

Swirl: The second consideration is swirl, the non-axial component of the flow on the engine face. It is caused by secondary flows within the duct, particularly those

set up by the first bend⁹. In experiments by Meyer et al.¹³, twin vortices generated by a delta wing placed in front of the compressor face were found to reduce surge margin by 26%, and compressor efficiency by 7% due to changing the nominal incidence angle of the flow on the first compressor (or fan) stage from design conditions¹⁴. It is measured by the maximum swirl angle, α_{max} , the worst 60° sector distortion coefficient, SC(60), and the average swirl intensity, SI_{avg} ¹⁴.

Total pressure distortion: The third aspect is distortions in the total pressure field at the engine face. These are caused by secondary flows and separations within the S-duct. They can lead to fan and compressor blade fatigue, and reduce the surge margin of the compressor¹². The descriptors used in papers by Asghar et al.^{1,3,15,16} are used here for the sake of easy comparison with experimental data. For all the distortion coefficients discussed in this report, a high value corresponds to a more severely distorted AIP. A simple metric is the worst 60° sector distortion coefficient, DC(60)⁹. More complex coefficients include the circumferential distortion coefficient, $(\Delta PC/P)_{avg}$, and the radial distortion coefficient, $(\Delta PR/P)_{max}$ ^{3,9,15}.

Vortex generators and boundary layer fences

Typical vortex generators (VGs) are a passive flow control (PFC) method that take the form of either vanes or ramps, with their tips located just outside of the boundary layer to allow for the greatest interaction between low momentum fluid in the boundary layer and the stream-wise vortices generated by the VGs. The vortices are highly effective in adverse pressure gradients and strong secondary flows. They work by entraining high momentum fluid into the boundary layer, and thus delaying separation⁶. The potential gains with the application of VGs are shown in many papers. Allan et al.¹⁷ found that they can reduce $(\Delta PC/P)_{avg}$ by 80%, and decrease DC(60) from 64% to 3.5% in a boundary layer ingesting inlet. Tanguy et al.¹⁸ achieved a 50% reduction in SI_{avg} and DC(60) and a 30% decrease in γ_{avg} , although there was some local increase in α . They also found that there was a strong dependence between VG performance and VG height. Tournier⁴ observed that VGs are most effective when orientated to produce co-rotating vortices that oppose near-wall secondary flows. The disadvantage of using VGs is that they are a source of parasitic drag, and are vulnerable to damage from foreign object ingestion^{6,19}.

Boundary layer fences and fins also reduce the intensity of secondary flows by blocking or redirecting the low momentum fluid in the near wall region⁹. Parham et al.⁵ were able to lower DC(60) by 11% with these PFC measures, but also found that they increased γ_{avg} by 52%. Results for a duct with an asymmetric boundary layer (and resulting bulk swirl) presented by Seddon report a reduction in SC(60) of almost 100%, provided that the fence is situated where crossflow velocities are high⁹.

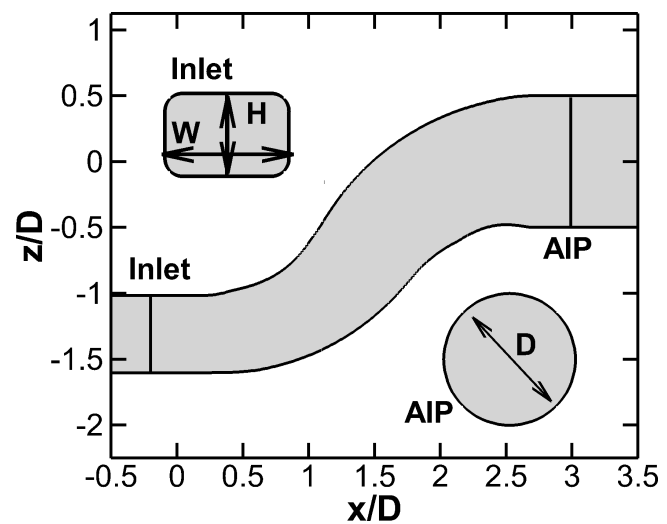
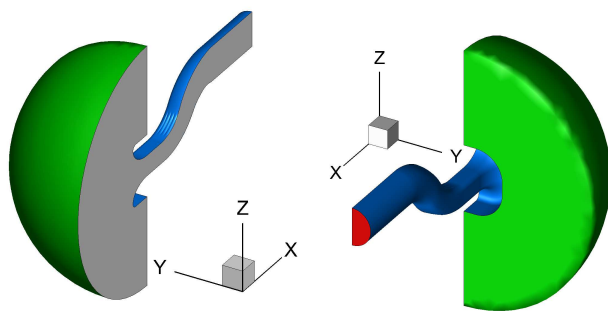


Figure 3. Duct dimensions and nominal inlet and AIP locations.

Experimental method and tubercle background

A schematic of the RMC duct with the location of the nominal inlet plane and the AIP is shown in Fig. 3. The ducts in this report are considered in their belly-mounted orientation, with the inlet below the AIP. The AIP diameter, D is 0.1016 m, which along with a Mach number of 0.8 on the nominal inlet plane, gives a Reynolds number of 1.4×10^6 . The aspect ratio of the duct (W/H) is 1.49, and the area ratio between the inlet plane and AIP is 1.57. The duct offset (vertical distance from the centre of the inlet to the centre of the AIP) is $1.31D$. Steady experimental data from the RMC Transient Transonic Wind-tunnel is available for wall static pressure taps on the top and bottom meridian of the duct, and total pressure probes from a 5-probe rotating rake on the AIP. The Transient Transonic Wind-tunnel is an indraft tunnel; ambient air is drawn through the bell mouth and duct, the outlet of which is connected to a valve and vacuum tank. The reader is referred to Asghar et al.³ for more detail on the experimental methodology.

Tubercles are a novel bio-inspired PFC method that work by generating counter rotating vortices that re-energise the boundary layer in a similar manner to VGs, delaying separation. They have been demonstrated successfully in external flow on the suction surfaces of wings, hydrofoils, and wind turbine blades²⁰. As well as a baseline duct with no tubercles, three ducts with different tubercle geometries were simulated - these are denoted by FC1, FC2, and FC3 (see Fig. 1). The tubercles in FC1 and FC2 have sinusoidal cross sections. FC1 has a larger amplitude and wavelength, and FC2 is stream-wise longer. FC3 has the same stream-wise length as FC2, but has shallower valleys. During experiments, FC1 was found to give earlier separation, this was hypothesised to be because the deep valleys were concentrating low-momentum fluid, leading to the shallower tubercle amplitude in FC2. FC3 extends this principle further, leading to a sinusoidal tubercle



Colour	Type	Values
Green	Pressure inlet	Total pressure = 1 bar, TI = 0.1%, TVR = 0.1.
Red	Pressure outlet	Average static pressure.
Blue	Wall	Zero-slip.
Grey	Symmetry	Zero-gradient.

Figure 4. Simulation boundary conditions.

profile being abandoned. For full details of the tubercle geometries, see Asghar et al¹.

CFD methodology

Boundary conditions

The boundary conditions used in the computations are shown in Fig. 4. The results were insensitive to the assumed turbulence intensity (TI) and viscosity ratio (TVR) at the domain inlet. This was because the domain inlet turbulence had decayed significantly by the time it was convected to the duct inlet, leading to turbulent production from the duct walls being the dominant source of turbulence within the duct. Total pressure sweeps were conducted on the pressure outlet to give an area averaged Mach number of 0.8 on the nominal inlet plane. Total pressures of around 0.825 bar were found to be a good starting point; generally only two or three sweeps were needed before the required Mach number was reached. The duct is symmetrical about the XZ-plane, so only half the duct was meshed to reduce computational requirements.

Mesh

Pointwise v18 was used to generate the meshes. An example mesh is shown in Fig. 5 for duct FC3, which was the most challenging duct to mesh due to the high curvature on the tubercle peaks. The domain volume was filled using an 8-10 million cell hybrid mesh with a 50 or 64 cell thick hexahedral boundary layer, with the wall adjacent cell height set to $0.8 \mu\text{m}$ to give a y^+ of less than 1. The 64 cell boundary layer (and 10 million cell mesh) was used with the FC ducts to better resolve the flow downstream of the tubercles. The smooth change in cell size between the hexahedral and tetrahedral zones of the hybrid mesh is shown on the symmetry plane in Detail A, Fig. 5. The surface mesh was clustered circumferentially towards the top and bottom meridians, primarily to provide sufficient geometric resolution to smoothly resolve the tubercles, although it also improved the resolution of the generated flow features.

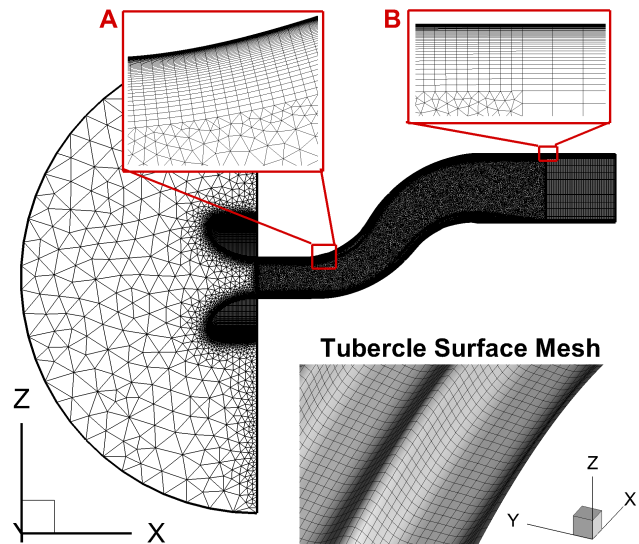


Figure 5. FC3 mesh.

The pressure inlet had a radius of $3D$, which was found by computations on similar ducts by Asghar et al.³ to be sufficiently large to not affect the solution. Similarly, the duct outlet was extruded for a further $1D$ down stream to avoid interactions with the pressure outlet boundary condition affecting the AIP. Extending this to $3D$ was found to make no difference to the results. The transition between the hybrid mesh and the prism extrusion is shown in Detail B, Fig 5.

The mesh used was finer than meshes used by Asghar et al.^{3,15}, which have been shown to give mesh independent solutions on similar transonic S-ducts. Using a coarser tetrahedral mesh was found to give the same solution, but made little difference in solution time due to convergence issues associated with the pyramid cells used to transition between the structured boundary layer mesh and the tetrahedral cells in the unstructured mesh. Computations on an fully hexahedral OH-grid mesh for FC1 gave near identical simulated flow fields, so the extra meshing time required was not justified for the other ducts. All results presented in this paper use hybrid meshes.

Solver settings

The Reynolds-Averaged Navier-Stokes (RANS) equations were solved using the pressure based solver in ANSYS Fluent 15.0. Pressure-velocity coupling was done using the SIMPLE algorithm. Default under relaxation factors were used for all solver variables except energy, this was reduced from 1 to 0.95 to prevent the temperature from diverging in the first few iterations. Second order upwind discretisation was used for all variables in the final solution, the first 2000 iterations were run with the first order upwind discretisation on the turbulent flow variables to aid solution stability. Good convergence (scaled residuals $< 5 \times 10^{-5}$ for continuity, and $< 1 \times 10^{-5}$ for all other variables) was achieved for all simulations. An ideal gas model for air was used, and the effects of viscous heating were included.

Results - RANS modelling investigation

Computations were carried out using two different RANS turbulence models: Menter's hybrid SST Linear Eddy Viscosity Model (LEVM)²¹, and the realisable $k-\varepsilon$ LEVM of Shih et al.²². The simulations were then validated against the experimental data of Asghar et al.¹. Duct FC1 was used as a representative environment for transonic S-ducts with passive flow control.

Shear Stress Transport (SST) model

The SST LEVM uses the Wilcox $k-\omega$ (WKW) model near walls, and the standard $k-\varepsilon$ (SKE) model elsewhere²¹. The SST model attempts to model some of the effects of Reynolds' stress anisotropy within the form of an LEVM by using Bradshaw's assumption that the Reynolds' shear stress in a boundary layer is proportional to the turbulent kinetic energy k , according to $-\overline{u'v'} = \rho a_1 k$ with the constant $a_1 \approx 0.31$ ²³. It is not desirable to use this equation away from walls, so the turbulent viscosity is calculated as

$$\mu_t = \frac{\rho a_1 k}{\max(a_1 \omega, SF_2)} \quad (2)$$

where F_2 is a blending function that equals one from the wall through to past the wake region of the boundary layer and zero in the free-stream, and S is the strain rate magnitude²¹. In this way, the model effectively limits the turbulent shear stress in the boundary layer and adverse pressure gradient regions.

The wall static pressure coefficient is defined as

$$C_p = \frac{p_w - p_1}{p_{01} - p_1} \quad (3)$$

where p_w is the wall pressure, and p_1 is the average static pressure on the inlet plane. The C_p distribution predicted by the SST model and the Spalart-Shur curvature correction term²⁴ is shown in Fig. 6 (SST31). The large flat regions between $x/D = 0.5$ and $x/D = 1.5$ on the top meridian and after $x/D = 2.2$ on the bottom meridian indicate large regions of flow separation, which occurs earlier and recovers more slowly than indicated by the experimental data. The large decrease in C_p after $x/D = 2.5$ on the top meridian is due to the substantial flow blockage caused by the separated region on the bottom meridian accelerating the flow and reducing the static pressure. A similar effect from the over-prediction of separation on the top meridian is seen in the minima at $x/D = 1.9$ on the bottom meridian. The over-prediction of separation leads to an over-prediction of total pressure losses; the computation gives $\gamma_{avg} = 0.138$, which exceeds the experimental value of 0.062 by 122%.

The effect of SST stress limiting

The effect of the shear stress limiter is to reduce mixing of high-momentum free-stream fluid into the near-wall layer by turbulent diffusion, giving the model excellent performance for many canonical 2D flows²¹. However, the excessive strength of the stress limiter

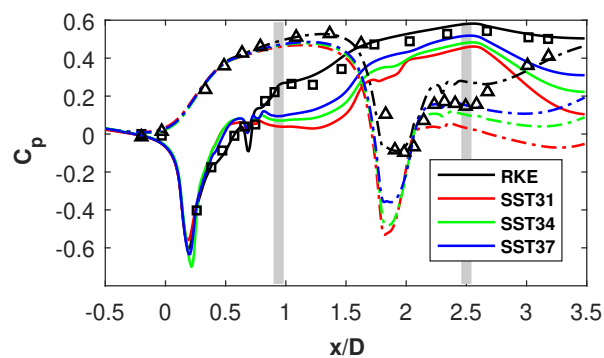


Figure 6. Static pressure distributions for duct FC1. SST31 indicates that $a_1 = 0.31$. Markers are experimental values from Asghar et al.¹. Solid lines/squares: top meridian. Dot-dashed lines/triangles: bottom meridian. Tubercle positions marked in grey.

in thick boundary layers and recirculating regions has been shown to cause an over-prediction of separation in flows such as asymmetric diffusers²⁵, transonic shockwave/turbulent boundary layer interactions^{26,27}, and wing-body junctions²⁸.

The value of a_1 was increased in 0.03 increments up to 0.40. The potential need for adjustments of this kind was noted when the model was introduced by Menter²¹. With reference to Fig. 6 (SST34 and SST37), it can be seen that this markedly improves the behaviour of the SST model. The onset of separation is now predicted more accurately, with $a_1 = 0.37$ matching experimental onset of separation almost exactly on the bottom meridian, although recovery is still delayed. On the top meridian, separation is still predicted early, but the wall static pressure recovers to almost match the experimental data until the effect of the blockage caused by the delayed recovery on the bottom meridian bend becomes significant after $x/D = 2.5$. The effects of the tubercles on the first bend are not resolved, as they lie within the excessively large computed separated region.

Diminishing returns from further increasing a_1 are evident in the values of γ_{avg} , which decreases rapidly initially, with $\gamma_{avg} = 0.133$ for $a_1 = 0.34$, but then stabilises when $a_1 = 0.37$ and 0.40, which both give $\gamma_{avg} = 0.110$. This has also been observed by Georgiadis and Yoder²⁷, where increasing a_1 beyond 0.37 had no effect, as the stress limiter was no longer reached. Therefore, stress limiting is not wholly responsible for the unsatisfactory results.

Further investigation found that the inclusion of the curvature correction negatively affected results. Although one would expect the curvature correction to improve the results around the tubercles, it causes the separated regions of the flow to increase in axial extent due to the suppression of turbulent production in regions of convex curvature on the inside of the bends^{23,24}. When the curvature correction was removed, γ_{avg} improved from 0.110 to 0.105 with $a_1 = 0.37$. Laminar-turbulent boundary layer transition modelling did not change results, as transition occurs very early on within the duct. Further improvements (at the cost

of decreased generality) could be made by calibration of the coefficients in the dissipation rate equation of the SST model in WKW mode - the standard values lead the model to predict a low μ_t , sensitising the SST model further to adverse pressure gradients, even when the stress limiter is not reached²⁵.

Realisable k - ε (RKE) model

The RKE LEVM model proposed by Shih et al.²² has two key differences to the SKE model: a stress limiter and an alternative formulation for the ε equation (based on the mean square vorticity fluctuation), which is a large source of error in the SKE model, particularly in separated, highly strained, or rotating flows²². A realisable model is one that will only predict physically tenable Reynolds stress fields. There are two conditions for realisability to be satisfied, positivity of normal Reynolds stresses, and the Schwarz inequality:

$$\left\{ \frac{\overline{u'v'^2}}{\overline{u'^2} \overline{v'^2}}, \frac{\overline{v'w'^2}}{\overline{v'^2} \overline{w'^2}}, \frac{\overline{u'w'^2}}{\overline{u'^2} \overline{w'^2}} \right\} < 1. \quad (4)$$

It is well known that the SKE model breaks these constraints in the case of large mean strain rate²². The stress limiter in the RKE model is formulated specifically to maintain realisability, and takes the form of a variable C_μ in the turbulent viscosity equation $\mu_t = \rho C_\mu k^2 / \varepsilon$ from the SKE model. In a non-rotating frame of reference, C_μ is given by

$$C_\mu = \frac{1}{A_0 + A_s U^{(*)} k / \varepsilon} \quad (5)$$

where A_0 is a constant, $U^{(*)} = \sqrt{S_{ij} S_{ij} + \Omega_{ij} \Omega_{ij}}$, S_{ij} is the rate-of-strain tensor, and Ω_{ij} is the vorticity tensor. A_s is a fairly complex function of the third invariant of the rate-of-strain tensor, $S_{ij} S_{jk} S_{ki}$ ²³.

Liou et al.²⁶ found that the model out performs the SST model in terms of mean-velocity profile and static pressure distribution for transonic bump flow, a test case that is held up as particularly suitable for assessing the performance of turbulence models in transonic separated flows. An additional advantage of the RKE model is that its stress limiter and response to curvature is very general, and derived from rigorous formalism, as opposed to ad-hoc empirical corrections as in the SST model²³.

Fig. 6 shows that the RKE model performs much better than the SST model for FC1. Excellent agreement with experimental static pressure data is achieved on the top meridian, and on the bottom meridian, the only discrepancy between the computation and experiment is the slightly late onset of separation at $x/D = 2.2$, which causes an elevated static pressure in the separated region due to the diffusion in the duct. Despite this, losses are predicted well, giving a γ_{avg} of 0.064, which is 3% above the measured value.

The dominant reason for the difference in the quality of predictions is the stress limiter of the SST and RKE models. For instance, when a_1 in the SST model was set to 0.31, the maximum value of μ_t in the domain was

0.0848 Pa·s, which is much lower than the maximum value of 0.298 Pa·s computed by the RKE model. As a higher μ_t stabilises the boundary layer, the effect of the severity of the SST stress limiter becomes clear.

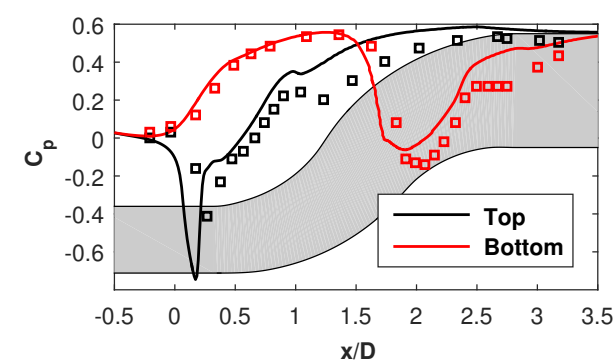
The results in this section illustrate that the RKE model is clearly the best model considered - it gives the most accurate results, and does not need stress limiters and other coefficients to be calibrated to match the experimental results. As a result of this, the RKE model has been used for all further computations in this paper.

Results - static pressure distributions

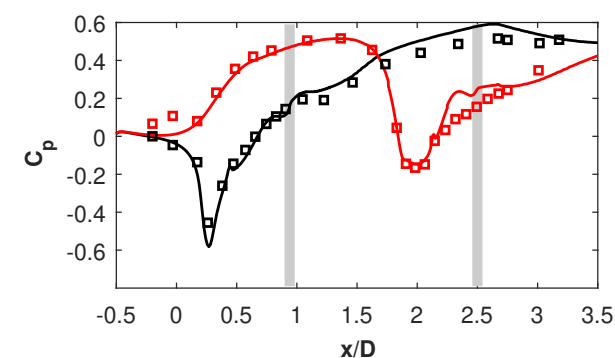
The distribution of C_p on the top and bottom meridian is plotted in Fig. 7 for the remaining three ducts. The typical behaviour described by Whitelaw and Yu⁸ is observed here; after a small region of constant velocity, the top meridian shows a rapid acceleration, corresponding to a decrease in the static pressure, followed by diffusion through the rest of the duct. The bottom meridian exhibits a region of deceleration in the first bend, followed by an acceleration in the second bend¹. The initial sharp decrease in static pressure at $x/D = 0.25$ on the top meridian has been observed for other ducts with high subsonic inlet velocities by, for example, Asghar et al.^{3,15}, and Tournier⁴. Tournier found that this was due to the flow in the inlet becoming choked after the bell mouth. In the RMC ducts it is a local effect, as only the flow on the top meridian is accelerated by the duct curvature.

Baseline duct: Fig. 7a shows the static pressure distribution for the baseline. This computation achieved the poorest agreement with experimental data, this is seen in three key areas. First, the flow acceleration on the top meridian occurs early, and the flow begins to diffuse earlier, leading to an elevated static pressure on the top meridian down-stream (compared to experimental data). Second is that recovery is predicted too soon after the first bend - separation is evident in the inflexion in the experimental static pressure between $x/D = 0.9$ and 1.5 on the top meridian - the computation predicts the axial position of the onset of separation well (although it overestimates the static pressure), but recovers by $x/D = 1.1$. This leads to even more excessive diffusion, and an over estimation of C_p at the AIP. The third feature is the late onset of separation and very rapid recovery after the second bend around $x/D = 2.8$ on the bottom meridian. Experimental data indicates that this should occur between $x/D = 2.5$ and 2.8. There are implications for the accuracy of results presented later in this paper, as the wake from the separation is the dominant feature on the bottom half of the total pressure distribution on the AIP, and the top-bottom pressure differential is the driver for the swirl flows.

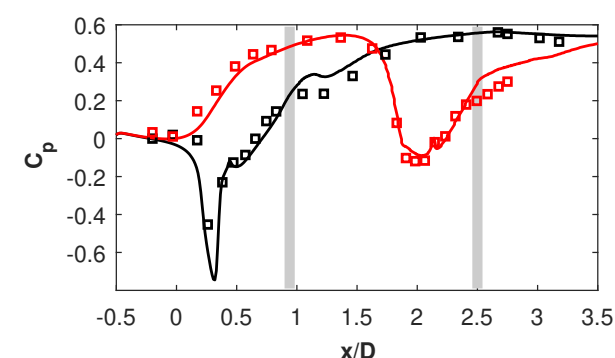
Duct FC1: In Fig. 6 (RKE), it can be seen that the static pressure distribution for FC1 is similar to that of the baseline duct, although the experimental data shows that the tubercles have achieved more rapid recovery and more gradual diffusion through the first bend, and earlier separation and recovery after the second bend¹. This improvement in S-duct performance is not reflected



(a) Baseline (Duct XZ-plane cross-section in background.)



(b) FC2 (Tubercle positions marked in grey.)



(c) FC3 (Tubercle positions marked in grey.)

Figure 7. Static pressure distributions on the top and bottom meridians. Markers are experimental values from Asghar et al.¹.

in the computational results due to the extent of the separated region being under-predicted in the baseline simulation. The earlier occurrence of separation on the second bend compared to the baseline is due to the collection of low momentum fluid in the large valleys between tubercles; this effect is mentioned briefly by Asghar et al.¹ and is investigated further later.

Duct FC2: The distribution shown in Fig. 7b shows an improvement over both the baseline and FC1. The separated region on the first bend extends from $x/D = 1.05$ to 1.2 (compared to 0.9 to 1.5 on the baseline duct). On the second bend, the separated region has been eliminated almost entirely in the experimental data, although there is a large difference between the top and bottom meridian, indicating poor flow uniformity on the AIP¹. The elimination of the second separated region is not observed in the computational results; a

separation region similar to duct FC1 is observed in these. Recovery after the second bend is predicted well, although the wake from the separated region will affect the accuracy of the AIP total pressure distribution.

Duct FC3: Referring to the experimental data in Fig. 7c, it can be seen that FC3 performs in very similar manner to FC2, with the only major advantage being the smaller difference between the top and bottom meridians at the AIP¹. The accuracy of the computational results is similar to the baseline although better general agreement is achieved; the static pressure is slightly over-predicted after both bends.

The reason for the poor predictions in the baseline duct in comparison to the other ducts is the effect of the valleys. In the FC ducts, the valleys rapidly concentrate low-momentum fluid, triggering separation. As this is a geometric effect that is present in the experimental data the computational separation still occurs in roughly the correct place in these ducts. In comparison, in the baseline duct, there are no valleys, meaning that the onset of separation is solely governed by the effects of the turbulence modelling.

Results - swirl

Although no experimental data is available for this variable, swirl is discussed here, as aside from its importance from an engine integration standpoint, it is the secondary flows that manifest themselves as swirl on the AIP that cause much of the total pressure distortion. The distribution of the swirl angle, α is shown in Fig. 8, and swirl metrics are shown in Table 1.

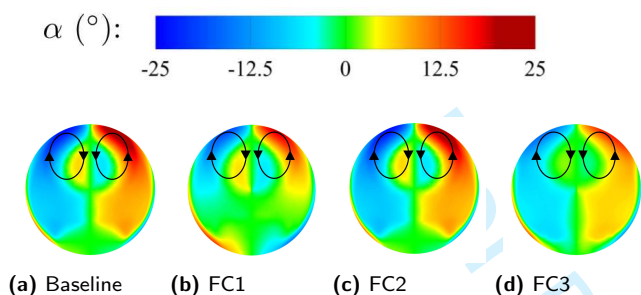
The swirl distributions in Fig. 8 qualitatively match what one would expect from the intrinsic S-duct flow regime discussed earlier⁸⁻¹⁰. Comparison with Particle Image Velocimetry (PIV) studies²⁹ and turbulence-resolving simulations^{14,30} on other S-ducts show a similar flow structure on the AIP, and similar values of coefficients, giving confidence that these results are in the correct neighbourhood.

Considering the right hand side of the plots, in the sector between the 12 o'clock and 2 o'clock positions, the Dean vortices that have persisted from the first bend are visible, with the flow towards the top meridian causing the maxima in α at the 1 o'clock position, then returning down the duct centreline, and then migrating outwards towards the duct walls. Also visible is some flow being driven towards the bottom meridian in the sector between the 3 o'clock and 6 o'clock positions. The baseline, FC2, and FC3 have these features directly adjacent to flow residual from the first bend returning to the top meridian; a long narrow vortex occurs in this region.

The values of α_{max} and $SC(60)$ are both governed by the magnitude of the maxima in the swirl at the 1 o'clock position noted above, although the negative swirl region where the Dean flow is returning to the duct wall offsets this slightly in the $SC(60)$ coefficient. The baseline duct is predicted to perform the best in this regard by the simulation, and FC2 the worst. SI_{avg} considers the entire AIP, not just localised areas, hence

Table 1. Computed and experimental S-duct performance metrics. Experimental values from Asghar et al.¹.

		Swirl			Total pressure			
		α_{max}	SC(60)	SI_{avg}	γ_{avg}	DC(60)	$(\Delta PC/P)_{avg}$	$(\Delta PR/P)_{max}$
Baseline	Comp.	12.0°	0.213	3.27°	0.052	0.466	0.063	0.043
	Exp.	-	-	-	0.064	0.353	0.038	0.038
	R.E.	-	-	-	-19%	+32%	+67%	+12%
FC1	Comp.	18.3°	0.330	4.16°	0.064	0.233	0.071	0.016
	Exp.	-	-	-	0.062	0.269	0.036	0.033
	R.E.	-	-	-	+3%	-13%	+111%	-53%
FC2	Comp.	23.2°	0.429	6.77°	0.067	0.207	0.081	0.015
	Exp.	-	-	-	0.067	0.286	0.036	0.033
	R.E.	-	-	-	0%	-28%	+126%	-54%
FC3	Comp.	14.5°	0.259	4.56°	0.057	0.440	0.072	0.047
	Exp.	-	-	-	0.063	0.252	0.035	0.032
	R.E.	-	-	-	-10%	+75%	+51%	+46%

**Figure 8.** AIP swirl angle as viewed from downstream. Anticlockwise flow is positive.

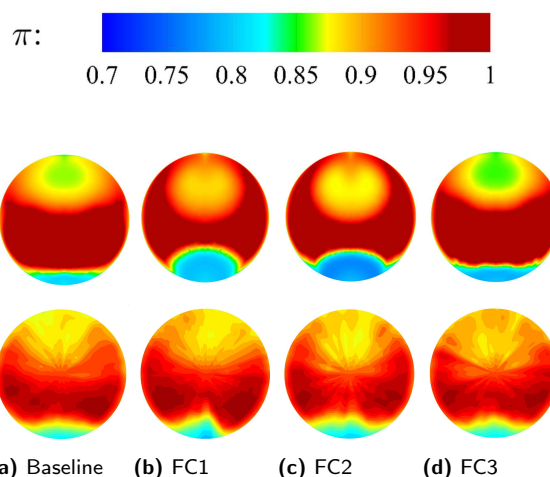
it does not follow the same trend as the other two coefficients. In particular, FC1 has a lower average swirl intensity than FC3. This is due to the bottom half of the AIP of FC1 exhibiting very little swirl, whereas in FC3 this region is dominated by flow residual from the first bend heading to the top meridian (see Fig. 8b,d). The larger profile of the tubercles on the first bend in FC1 seems to suppress the formation of Dean vortices, leading to a reduced SI_{avg} .

It is likely that the computations have under-predicted the swirl velocities for the baseline and to a lesser extent, FC3. In the first bend in these ducts, the difference in static pressure between the top and bottom meridian has been under-predicted by the CFD (Figs. 6,7). It is this pressure differential that is responsible for the formation of the Dean vortices, the dominant feature of the swirl distributions on the AIP, so its under-prediction implies that the swirl has also been under-predicted.

Results - total pressure distortion and losses

Total pressure ratio distribution

The computational and experimental distribution of the total pressure ratio, $\pi = p_0/p_{01}$, on the AIP is shown in Fig. 9 for all four ducts. The plots all show the same three distinct regions: a medium total pressure region ($0.85 < \pi < 0.90$) around the top meridian, a high total pressure region ($\pi > 0.96$) that spreads laterally across the entire AIP at its vertical centre, and a low pressure region ($\pi < 0.82$) at the bottom meridian. The geometry and severity of the three regions varies considerably

**Figure 9.** AIP total pressure ratio. Top: computational results. Bottom: experimental results from Asghar et al.¹.

depending on the duct, so they are discussed on a region-by-region basis below:

Medium total pressure region: This region consists of a central stem at the top meridian, and two lobes, which are indicative of the Dean vortices. The total pressure ratio is low in this region because the Dean vortices, aside from generating internal losses through viscous dissipation, entrain low energy fluid from the boundary layer and the edge of first separated region. The ducts are split into two groups here: baseline and FC3, and FC1 and FC2. The total pressure in this region is higher in the latter group, this is due to the more severe maximum swirl (up to 42% of the average axial velocity for FC2) leading to a higher velocity magnitude, and thus a higher total pressure.

The exact location of the Dean vortices is not visible in the experimental data, and the total pressure in their cores is higher than in computations, particularly for the baseline and FC3. For example, the computations on FC3 found $\pi = 0.84$ in the Dean vortex cores, whereas the experimental data gives $\pi \approx 0.89$. This might indicate some degree of unsteadiness in the Dean vortices' position that was not captured in the simulation - if they were to move around, the time averaged total pressure of this location would be

increased by higher total pressure regions moving over it.

Low total pressure region: The separated region from the second bend (and its associated reversed flow and high losses) extends beyond the AIP for all ducts. In comparison to the baseline, this region is computed to have a greater vertical extent in FC1 and FC2 - this is due to the greater stream-wise length of the separated region discussed earlier. FC2 and FC3 display small regions of low total pressure being drawn up the wall from the bottom to top meridian. This can be explained with reference to the location of the regions of high swirl returning flow to the bottom meridian in Fig. 8 - in FC1, they are much closer to the bottom meridian, and so act to oppose the lateral spread of the separated region.

The size and severity of the low pressure region is over-predicted in the simulations, and there are significant asymmetries in the experiment that are not present in the computations. The asymmetries imply two things: that insufficient time-averaging was conducted in the experiment (noted by Asghar et al. in previous S-duct experiments³); and/or that the time-averaged effects of the unsteady flow in the separated region were not captured in the simulation¹⁴.

High total pressure region: Made up of effectively inviscid core flow, the shape of this region is dictated by the boundaries of the two regions discussed above. The upper boundary of this region is delineated much more sharply in FC1 and FC2. In these ducts, high momentum fluid is still being entrained into the Dean vortices; this is visible in the "fingers" of dark red pointing towards the top meridian in Figs. 9b,c. This region has a higher total pressure than experimentally observed, so will compensate for the other regions when γ_{avg} is considered.

Loss and distortion coefficients

A better understanding of the accuracy of the simulation data can be gained by calculating loss and distortion coefficients from the data in Fig. 9 for a quantitative comparison. A summary of these coefficients is shown in Table 1, and the results are plotted in Fig. 10. The general trend is that the CFD fails to capture the ranks of the designs, this is particularly true for the distortion coefficients. The relative error (R.E.) is defined as

$$R.E. = \frac{\phi_{comp} - \phi_{exp}}{\phi_{exp}}, \quad (6)$$

where ϕ_{comp} and ϕ_{exp} are the computational and experimental values of the parameter ϕ . Calculations were carried out on 5 equal area rings, split into 18 and 72 circumferential points (the former was used by Asghar et al.¹) to check for dependency on the measurement resolution, very little dependence was found; the results from the latter grid are presented here.

γ_{avg} : This has been predicted with good accuracy for all ducts, but particularly FC1 and FC2. The largest relative error is -19% for the baseline duct, indicating

an under-prediction of losses as one would expect from the discussion of Fig. 7a. In both the computation and the experiment, the highest losses are found in FC2. However, the rank of the other three ducts has not been predicted accurately by the CFD; this is primarily due to the underprediction of losses in the baseline duct and FC3. The loss coefficient is extremely sensitive - whilst the -19% error sounds large, Eqn. 1 shows that it corresponds to a relative error of +1.2% in π_{avg} .

DC(60): The experimental trend that the addition of tubercles decreases DC(60) was observed in all simulations except for duct FC3; where it was over-predicted by 75%. This is due to the under prediction of p_0 in the Dean vortex cores at the top meridian. DC(60) selects different sectors for the ducts (the 12 o'clock to 2 o'clock sector for the baseline and FC3, and the 4 o'clock to 6 o'clock sector for FC1 and FC2), showing that it is very sensitive to local total pressure variations. This has been noted by other authors, such as Berens et al.³¹.

$(\Delta PC/P)_{avg}$: This distortion coefficient is systematically over-estimated and fails to predict the rank of any of the designs, and is the most poorly predicted. It is dominated by the effects of the lateral extent of the low pressure region, which, as noted earlier, is over-predicted in the simulations. To check this coefficient, it was compared with the Circumferential Distortion Index (CDI) used by MacManus et al.¹⁴; an identical trend was observed.

$(\Delta PR/P)_{max}$: This occurred in the outermost ring for all ducts. Agreement with experimental values and ranks was poor, with the radial distortion being under-predicted for FC1 and FC2 due to high total pressure in the fingers and high-velocity core, and over-predicted for the baseline and FC3 due to the low total pressure in the Dean vortex cores. To check this coefficient, it was compared with the Radial Distortion Index (RDI) used by MacManus et al.¹⁴; an identical trend was observed.

RANS methods and distortion prediction

Although the RKE turbulence closure has been found to satisfactorily reproduce static pressure distributions, the results presented in this section show that they do not give results or ranks for the total pressure distortion. Two unsteady effects dominate the dynamic behaviour of the flow inside S-ducts. The first is the unsteadiness of the separated regions downstream of both bends. The second is a related phenomenon called swirl switching, intrinsic to internal flows in curved pipes. This is where the Dean vortices alternately dominate the flow within the duct, changing the dominant swirl direction at the AIP. Proper Orthogonal Decomposition studies on PIV and Delayed Detached Eddy Simulation (DDES) data have found that the reason for the existence of this is due to the formation of instabilities in the shear layer and separated region after the first bend^{30,31}. In high-offset ducts such as the ones considered in this report, the distinction between these two mechanisms is unclear and their characteristic frequencies are broadband, although they are still present¹⁴.

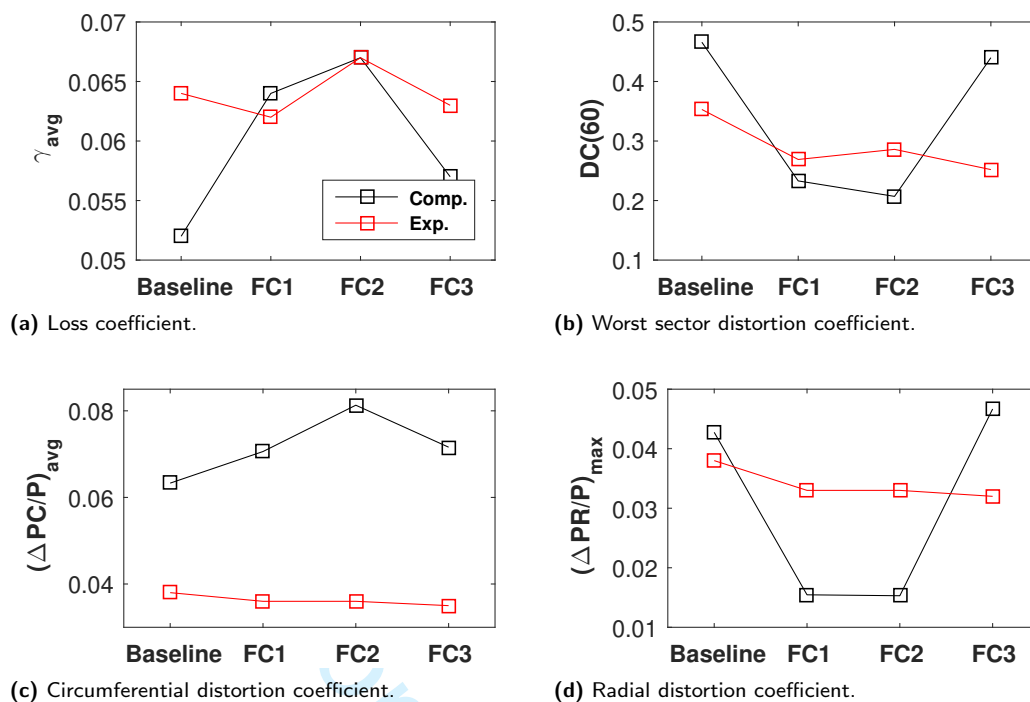


Figure 10. Performance metric plots. (Data from Table 1.)

Unsteady RANS (URANS) computations were carried out using the hybrid mesh of duct FC1 with time steps ranging from $2.5 \mu\text{s}$ to 0.2 ms for a total of 40 flow through times. The peak value of π was 0.001 above the average (compared to 0.026 above the average in DDES data from MacManus et al.¹⁴), indicating no significant unsteadiness. This is due to the unsteadiness being inherently asymmetric, and thus prohibited by the presence of the symmetry boundary condition. It is unlikely that an improvement in results would have been obtained in a full duct URANS simulation - the time and length-scales of shear layer instabilities are not resolved by URANS models and the flow field lacks the clear spectral gap.

Results - mechanisms of tubercles as passive flow control

Vortex generation

The computations show that the tubercles are successful in generating stream-wise vortices, although their energising effect on the boundary layer is expected to be localised - the vortices in the key regions at the top and bottom meridian are mixed out rapidly in the separation regions after each bend. Fig. 11 shows the X-vorticity (ω_x) distribution at YZ-plane slices distributed between the reference plane and the AIP.

Visible on the top meridian on plane A is the vorticity generated by the tubercles at the first bend transported down-stream. As separation occurs between planes A and B, these vortices have not yet been mixed out. The alternating positive and negative senses of the rotation of the vortices is consistent with counter-rotating vortices in experiments and simulations on

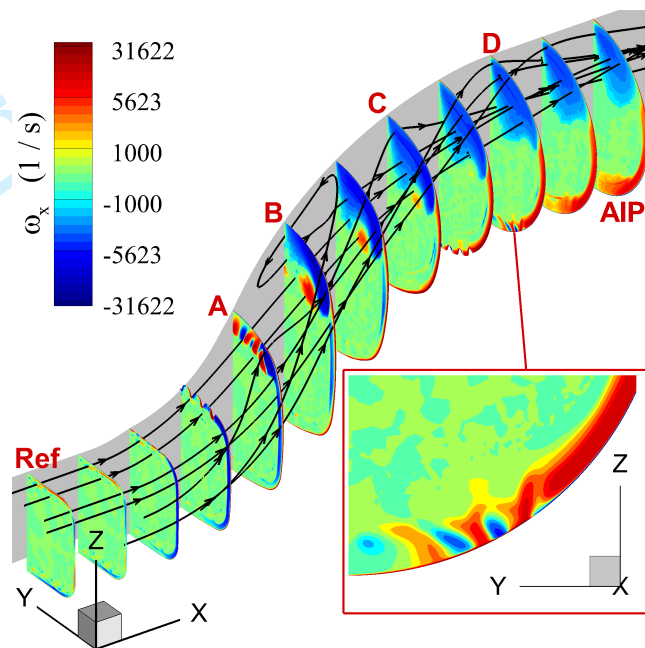


Figure 11. Streamlines and cross sections of X-direction vorticity for duct FC3. Inset: zoom of the bottom meridian on plane D.

tubercles in external flow²⁰. By plane B, the vortices in the centre of the duct have been mixed out due to the strong velocity gradients in the separated flow structure visible in the reversed streamline near the top meridian. The only vortex pair that is still visible is on the outside of the duct, avoiding the separated region. The vortex rotating in the negative sense is reinforced by the flow being driven from the bottom to the top meridian by the duct curvature. The positive vortex is

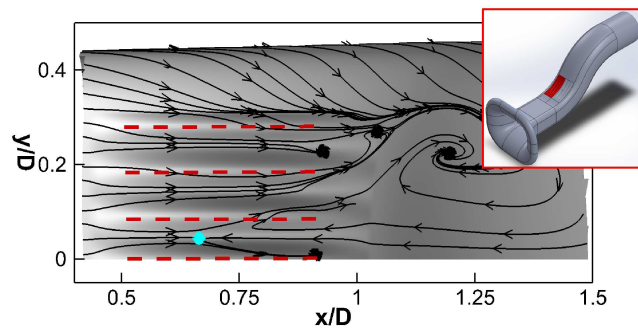


Figure 12. Skin friction lines for the top surface of the first bend for duct FC2. The blue dot indicates the saddle point, and red dashes indicate tubercle peaks. Inset: Plot location highlighted.

almost fully dissipated by plane C, and the negative vortex has begun to roll up into the Dean vortices.

At plane D, the vorticity generated by the second set of tubercles is seen. The discussion for this slice is similar to plane A, except for the fact that these vortices have already begun to be dissipated by other flow features in the duct, namely the separation region at the duct centre and the flow being driven towards the bottom meridian by the second bend. By the AIP, the Dean vortices and the secondary flow from the second bend dominate the vorticity distribution, although both features are altered by the tubercles.

Near-wall flow

The undesirable effect of deep valleys between tubercles was noted briefly by Asghar et al.¹. To investigate this further, skin friction lines, shown in Fig. 12 for FC2, have been used to investigate the near-wall flow. The presence of tubercles alters the flow topology at the onset of separation significantly - they deflect low momentum fluid into the valleys, thickening the boundary layer, and ultimately inducing earlier separation, as evidenced by the saddle point near the centre of the duct³². This explains the later onset of separation in FC3 compared to FC1 and FC2, as the profile of FC3 deflects less low momentum fluid into the valleys.

The blocking effect of the tubercle profiles in cross-flow is shown by the convergence of skin friction lines at $y/D = 0.30$. This was assumed to be a negative effect in Asghar et al.¹, and was a driver for the smaller amplitude of the tubercle peaks in FC2 and FC3, although it is actually a similar effect to the boundary layer fences discussed by Parham⁵ and Seddon⁹. This suggests that a large tubercle such as in FC1 may be desirable on the outside of the duct where it will act to suppress secondary flows, but undesirable in the centre of the duct where it will cause early separation. However, the tubercles are significantly stream-wise shorter than the fences reported by Seddon⁹, which extend for 75% of the first bend. This suggests that extending the tubercles in the stream-wise direction will improve their boundary layer fence effect.

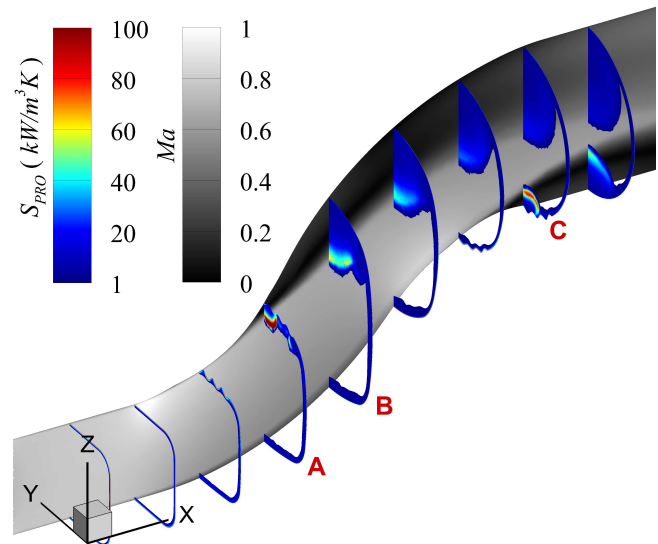


Figure 13. Local entropy production rate and Mach number for duct FC2.

Location of losses

Contours of the local entropy generation rate, \dot{S}_{PRO} , for FC2 are shown in Fig. 13. As per Kock³³, \dot{S}_{PRO} was split into viscous and heating effects, which were further split using the Reynolds decomposition into their mean-flow and fluctuating flow components, the latter being modelled using ε and the turbulent Prandtl number. Viscous losses from fluctuating flow components were dominant, exceeding heating losses from the fluctuating flow components by a factor of three, and mean-flow components by two or more orders of magnitude.

Three loss mechanisms are visible in Fig. 13: boundary layer losses, secondary flow losses from the Dean vortices, and wake losses from separated regions. The boundary layer losses are fairly constant between the ducts, being dependent on mean flow velocities (but still generate a lot of entropy - \dot{S}_{PRO} in these regions exceeds the scale of Fig. 13 by two orders of magnitude). The secondary flow losses are due to the Dean vortices, and are visible in the large regions on the top meridian at plane B. On the outside of the top of plane B is also the loss core from the vortex generated by the outermost tubercle. For the baseline the majority of the loss on planes A and B is in this region, before the Dean vortices track to the centre of the duct downstream. This does not imply that the tubercles have reduced the loss on these planes, just that they have moved the loss location. The losses within the separated regions seem to be the dominant factor differentiating between the ducts.

Conclusion

The flow within a transonic diffusing S-duct has been investigated computationally and compared to experimental data from Asghar et al.¹. Menter's SST²¹ model fails to reproduce pressure losses and wall static pressure distribution due to over-predicted separated regions caused by an over-active stress limiter. The RKE model²² fares better, but under-predicts losses for the

1
2 baseline duct and FC3, and fails to give accurate results
3 for the total pressure distortion.

4 Computed swirl distributions are found to reproduce
5 those observed in S-ducts by other authors, with Dean
6 flow from the first bend persisting to the AIP and
7 dominating. The larger profile of FC1 in cross flow is
8 found to act like a boundary layer fence, reducing the
9 average swirl. The RKE model predicts static pressure
10 distributions well, but fails to accurately predict the
11 ranks of all the coefficients calculated to evaluate
12 the design. Errors are particularly pronounced for the
13 total pressure distortion coefficients, with errors up to
14 +126%. More accurate prediction of the coefficients
15 requires that the unsteady effects in the separation
16 region on the first bend are captured. Despite this the
17 CFD results have proved to be useful for qualitatively
18 investigating the effect of the design interventions.

19 An improved design for the tubercles is proposed - this
20 involves having large tubercles such as FC1 on the side
21 to take advantage of their boundary layer fence effect,
22 while maintaining the use of the FC3 tubercles in the
23 duct centre for their suppression of separation through
24 boundary layer re-energisation.

25 Recommendations

26 Unsteady simulations are necessary to capture the
27 intrinsic unsteadiness of the flow within S-ducts.
28 URANS computations on half-duct geometries have
29 shown that there is little benefit to be gained in using
30 URANS models on the same geometry. Berens et al.³¹
31 have shown that little advantage can be gained with
32 URANS or DES simulations, even on a full duct.
33 The deficiency of DES is likely due to the models'
34 tendency to predict early, grid-induced separation. An
35 approach that addresses this is Delayed-DES (DDES).
36 DDES computations in similar ducts by MacManus et
37 al.¹⁴ predicted $(\Delta PC/P)_{avg}$ to within +23%, a marked
38 improvement on the RANS computations in this report
39 (between +51% and +126%).

40 Despite not capturing the unsteadiness and its effects
41 on total pressure losses or distortion, the RANS
42 simulations with the RKE model can be used as
43 a relatively low computational cost method to drive
44 design improvements in S-ducts with passive flow
45 control as it allows investigations of the local flow
46 structure over the tubercles.

47 Acknowledgements

48 The authors would like to thank William Allan, Marc
49 LaViolette, Asad Asghar, and Satpreet Sidhu from the Royal
50 Military College of Canada for generously sharing their
51 experimental results and the details of the S-duct geometries.
52 Thanks are also due to the anonymous reviewers for their
53 help in improving this paper.

54 References

55 1. A. Asghar et al., "Investigation of a passive flow control
56 device in an S-duct inlet of a propulsion system with
57

- 58 high-subsonic flow," *Proceedings of ASME Turbo Expo*
59 *2018*, 2018. GT2018-76636.
- 60 2. C. Fiola and R. Agarwal, "Simulation of secondary and
separated flow in a diffusing S-duct using four different
turbulence models," *Journal of Aerospace Engineering*,
vol. 228, no. 11, pp. 1954–1963, 2013.
3. A. Asghar et al., "Performance evaluation of an S-duct
diffuser of a flight-vehicle inlet in high-subsonic flow,"
Proceedings of ASME Turbo Expo 2015, 2015. GT2015-
43740.
4. S. Tournier, "Flow analysis and control in a subsonic
inlet," *Masters Thesis, MIT*, 2005.
5. J. Parham et al., "Flow control for boundary layer
ingestion in an S-duct diffuser," in *49th AIAA Aerospace*
Sciences Meeting, AIAA, 2011. AIAA 2011-822.
6. J. Vaccaro et al., "Experimental and numerical
investigation on steady blowing flow control within a
compact inlet duct," *International Journal of Heat and*
Fluid Flow, vol. 54, pp. 143–152, 2015.
7. D. Bingaman, "Performance study for inlet installa-
tions," 1992. NASA Contractor Report 189714.
8. J. Whitelaw and S. Yu, "Turbulent flow characteristics
in an S-shaped diffusing duct," *Flow Measurement and*
Instrumentation, vol. 4, no. 3, pp. 171–179, 1993.
9. J. Seddon and E. Goldsmith, *Intake Aerodynamics*.
AIAA Education Series, 1985.
10. E. Greitzer et al., *Internal Flow*. Cambridge, UK:
Cambridge University Press, 2004.
11. G. Gerolymos and I. Vallet, "Reynolds-Stress Model
Prediction of 3-D Duct Flows," *Flow, Turbulence, and*
Combustion, no. 96, pp. 45–93, 2016.
12. A. Sóbester, "Tradeoffs in jet inlet design: a historical
perspective," *Journal of Aircraft*, vol. 44, no. 3, pp. 705–
717, 2007.
13. W. Meyer et al., "The influence of intake swirl distortion
on steady state performance of a low bypass twin-spool
engine," *AGARD Report*, 1991. CP-498.
14. D. MacManus et al., "Complex aeroengine intake ducts
and dynamic distortion," *AIAA Journal*, vol. 55, no. 7,
pp. 2395–2409, 2017.
15. A. Asghar et al., "Entrance aspect ratio effect on S-duct
inlet performance at high-subsonic flow," *Proceedings of*
ASME Turbo Expo 2016, 2016. GT2016-57875.
16. A. Asghar et al., "Investigation of a passive flow control
device in S-duct inlet of a propulsion system with high
subsonic flow," in *CASI AERO17*, 2017.
17. B. Allan et al., "Optimal design of passive flow control
for a boundary-layer-ingesting offset inlet using design-
of-experiments," 2008. NASA/AIAA.
18. G. Tanguy et al., "Passive flow control study in an S-
duct intake using stereo particle image velocimetry,"
AIAA Journal, vol. 55, no. 6, pp. 1862–1877, 2017.
19. L. Jenkins et al., "Flow control device evaluation for an
internal flow with an adverse pressure gradient," in *40th*
AIAA Aerospace Sciences Meeting, AIAA, 2002. AIAA
2002-0266.
20. F. Fish et al., "The tubercles on humpback whales' flip-
pers: application of bio-inspired technology," *Integrative*
and Comparative Biology, vol. 51, no. 1, pp. 203–213,
2011.

21. F. Menter, "Improved two equation k- ω turbulence models for aerodynamic flows," *NASA Technical Memorandum 103975*, 1992.
22. T. Shih et al., "A new k- ϵ eddy viscosity model for high Reynolds number turbulent flows," *Computers and Fluids*, vol. 24, no. 9, pp. 229–238, 1995.
23. M. Leschziner, *Statistical Turbulence Modelling for Fluid Dynamics - Demystified*. London, UK: Imperial College Press, 2016.
24. P. Smirnov and F. Menter, "Sensitization of the SST turbulence model to rotation and curvature by applying the Spalart-Shur correction term," *Journal of Turbomachinery*, vol. 131, no. 041010, 2009.
25. D. Apsley and M. Leschziner, "Advanced turbulence modelling of separated flow in a diffuser," *Flow, Turbulence, and Combustion*, vol. 63, pp. 81–112, 1999.
26. W. Liou et al., "Turbulence model assessment for shock wave/turbulent boundary layer interaction in transonic and supersonic flows," *Computers & Fluids*, vol. 29, pp. 275–299, 2000.
27. N. Georgiadis and D. Yoder, "Recalibration of the shear stress transport model to improve calculation of shock separated flows," in *51st Aerospace Sciences Meeting*, 2013. NASA/TM-2013-217851.
28. D. Apsley and M. Leschziner, "Investigation of advanced turbulence models for the flow in a generic wing-body junction," *Flow, Turbulence, and Combustion*, vol. 67, pp. 25–55, 2001.
29. D. Gil-Prieto et al., "Convolved intake distortion measurements using stereo particle image velocimetry," *AIAA Journal*, vol. 55, no. 6, pp. 1878–1892, 2017.
30. D. Gil-Prieto et al., "Delayed detached-eddy simulation and particle image velocimetry of S-duct flow distortion," *AIAA Journal*, vol. 55, no. 6, pp. 1893–1908, 2017.
31. T. Berens et al., "Numerical simulations for high offset diffuser flows," Tech. Rep. NLR-TP-2014-096, National Aerospace Laboratory NLR, 2014.
32. J. Détery, "Robert Legendre and Henri Werlé: Towards the elucidation of three-dimensional separation," *Annual Reviews in Fluid Mechanics*, vol. 33, pp. 129–154, 2001.
33. F. Kock and H. Herwig, "Entropy production calculation for turbulent shear flows and their implementation in CFD codes," *International Journal of Heat and Fluid Flow*, vol. 26, pp. 672–680, 2005.

Appendix

Performance metric definitions

Swirl The maximum value of the swirl angle on the AIP is used as a metric for the swirl on the AIP¹⁴. The swirl angle is defined as

$$\alpha = \arctan(V_{\theta}/W_{avg}) \quad (7)$$

where V_{θ} is the circumferential velocity on the AIP (positive anticlockwise), and W_{avg} is the average axial velocity on the AIP¹⁴. The worst 60° swirl coefficient is calculated from

$$SC(60) = \frac{V_{\theta avg 60}}{W_{avg}} \quad (8)$$

where $V_{\theta avg 60}$ is the average of V_{θ} in the worst 60° sector¹⁴.

The final swirl metric used in this report is the average swirl intensity,

$$SI_{avg} = \frac{1}{5} \sum_{i=1}^5 \left(\frac{1}{360} \int_0^{360} \alpha_i(\theta) d\theta \right) \quad (9)$$

where the subscript i corresponds to one of the 5 equal area rings described by the path of one the probes on the pressure rake the experimental set-up of Asghar et al.¹, as is convention¹⁴.

Total pressure distortion $DC(\theta)$ measures the average total pressure in the worst sector of an angular extent of θ degrees ($p_{0\theta}$)⁹. It is defined as

$$DC(\theta) = \frac{p_{02} - p_{0\theta}}{p_{02} - p_2} \quad (10)$$

where p_2 is the average static pressure on the AIP. θ must be reasonably large; 60° is regarded as a minimum, and is also the most commonly used⁹.

The circumferential distortion coefficient is given by

$$(\Delta PC/P)_{avg} = \frac{1}{5} \sum_{i=1}^5 \left(\frac{p_{0i} - p_{0i,low}}{p_{0i}} \right) \quad (11)$$

where p_{0i} is the average total pressure in the i^{th} ring, and $p_{0i,low}$ is the average total pressure in all sectors of the i^{th} ring that have a total pressure lower than the ring average^{3,9,15}. The notation $DPCP_{avg}$ is sometimes used for this coefficient.

The final total pressure distortion coefficient used in this report is the radial distortion coefficient. It is defined as

$$(\Delta PR/P)_{max} = \max_{i \in [1,5]} \left(\frac{p_{02} - p_{0i}}{p_{02}} \right) \quad (12)$$

although it is sometimes notated as $DPRP_{max}$. The average of this coefficient across all five equal area rings is 0, so the maximum value, corresponding to the lowest average total pressure ring is used.

Nomenclature

A	=	tubercle amplitude
A_0	=	constant in the RKE model stress limiter
A_s	=	function in the RKE model stress limiter
a_1	=	constant in Bradshaw's assumption
C_p	=	wall static pressure coefficient
C_{μ}	=	constant in the turbulent viscosity equation
D	=	AIP diameter
$DC(60)$	=	worst 60° sector distortion coefficient
F_2	=	blending function in the SST model stress limiter
H	=	duct inlet height
k	=	turbulence kinetic energy
p_0	=	local total pressure
p_{01}	=	average inlet total pressure
p_{02}	=	average outlet total pressure
p_1	=	average inlet static pressure

1	
2	p_w = wall static pressure
3	$R.E.$ = relative error
4	S = strain rate magnitude
5	S_{ij} = rate-of-strain tensor
6	\dot{S}_{PRO} = local entropy generation rate
7	$SC(60)$ = worst 60° sector swirl coefficient
8	SI_{avg} = average swirl intensity
9	u, v, w = $x, y,$ and z velocity components
10	u', v', w' = fluctuations of $x, y,$ and z velocity
11	components
12	W = duct inlet width
13	x, y, z = Cartesian coordinates
14	y^+ = non dimensional wall distance
15	α_{max} = maximum swirl angle
16	γ_{avg} = average total pressure loss coefficient
17	$(\Delta PC/P)_{avg}$ = circumferential distortion coefficient
18	$(\Delta PR/P)_{max}$ = radial distortion coefficient
19	ε = dissipation rate of k
20	λ = tubercle wavelength
21	μ_t = turbulent viscosity
22	π = local total pressure ratio
23	π_{avg} = average total pressure ratio
24	ρ = density
25	ϕ = general parameter
26	ϕ_{comp} = computational value of ϕ
27	ϕ_{exp} = experimental value of ϕ
28	Ω_{ij} = vorticity tensor
29	ω = turbulence eddy frequency
30	ω_x = x component of the vorticity vector
31	
32	
33	
34	
35	
36	
37	
38	
39	
40	
41	
42	
43	
44	
45	
46	
47	
48	
49	
50	
51	
52	
53	
54	
55	
56	
57	
58	
59	
60	

RANS Modelling in Transonic S-Ducts with Passive Flow Control

Tom Hickling and Grant Ingram

S-duct diffusers are used in aircraft with embedded engines to route ambient air to the fan face. Sizing and stealth considerations drive a need for high curvature ducts, but the curvature causes complex secondary flows that lead to total pressure distortion and swirl velocities at the engine face. These must be controlled for stable engine operation. In this paper, tubercles, a novel bio-inspired passive flow control method, are analysed numerically in a duct with transonic flow. The results are compared to experimental data obtained as part of a campaign at the Royal Military College, Canada to investigate the effects of S-duct geometry and novel passive flow control devices on the performance of transonic S-ducts. The performance of RANS turbulence models in the S-ducts is assessed - Menter's SST model predicts excessive losses due to the over-activity of its stress limiter. The realisable $k-\epsilon$ model gives a significant improvement in the prediction of static pressure distributions, but losses and distortion characteristics are predicted poorly due to the model's inability to resolve the effects of unsteadiness in separated regions. Large tubercle geometries are found to trigger earlier separation in the centre of the duct by concentrating low momentum fluid in valleys, but they also act as boundary layer fences away from the duct centre. Smaller geometries are found to generate vortices that re-energise the boundary layer, delaying flow separation. Methods are recommended for future computational analyses of S-ducts and new designs of tubercles.

Introduction

This report discusses the use of computational fluid dynamics (CFD) to lend insight to experimental data on tubercles (a novel flow control device) in transitioning S-duct diffusers by Asghar et al. at the Royal Military College (RMC), Canada¹. Following an overview of the S-ducts and performance measures considered, this paper presents the computational methodology and five sections of results: an investigation of the performance of RANS turbulence models in the ducts; discussions of the static pressure, swirl, and total pressure distributions; and a more detailed analysis of the effects of tubercles on the flow field. Finally, suitable methods are recommended for future computations on S-ducts with passive flow control.

1
2
3
4
5
6
7
8
9
10
11
12
13
14
15
16
17
18
19
20
21
22
23
24
25
26
27
28
29
30
31
32
33
34
35
36
37
38
39
40
41
42
43
44
45
46
47
48
49
50
51
52
53
54
55
56
57
58
59
60

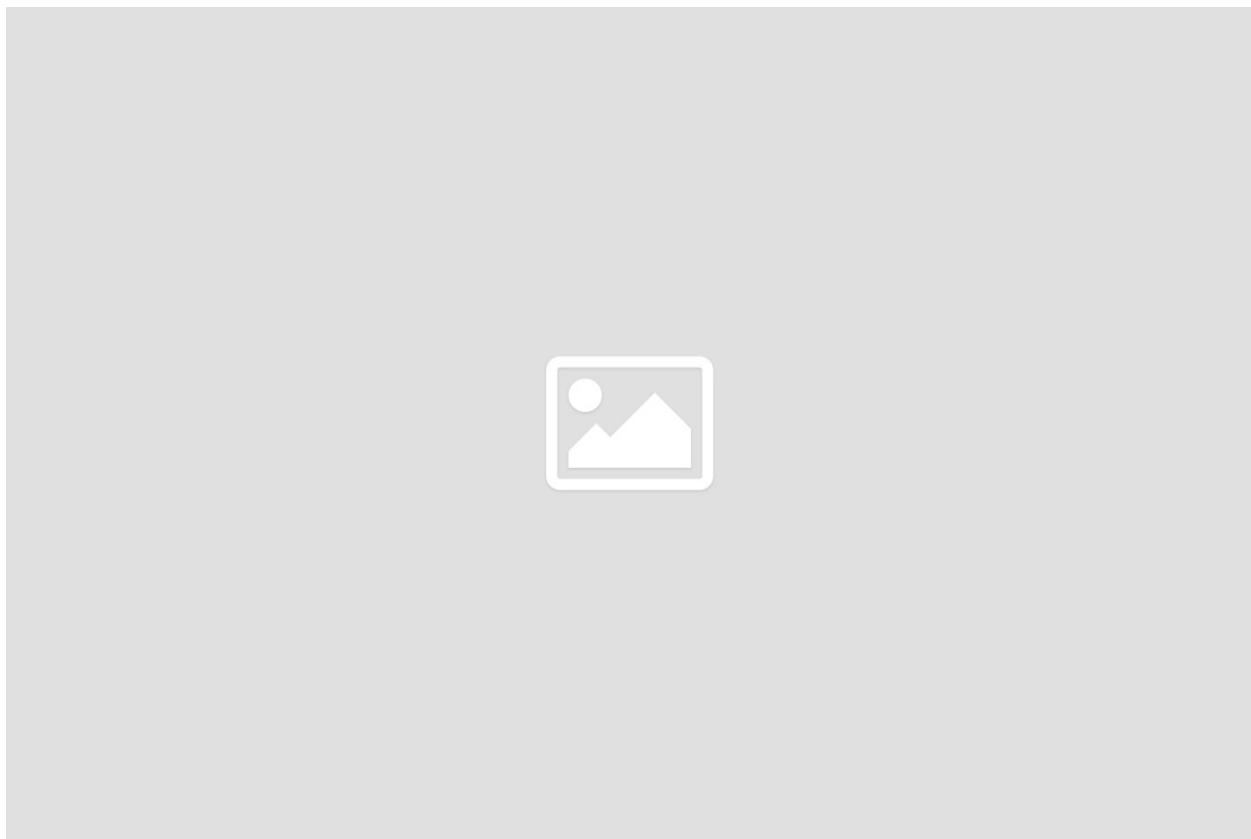


Figure 1. Isometric view of the RMC S-duct. Left: From above. Right: From below.

Review



Figure 2. Tubercle dimensions. D is the diameter of the duct outlet, 0.1016 m.

One of the ducts analysed is shown in Fig. 1, with the tubercle locations on the inside of both bends highlighted. The profiles and key dimensions (amplitude, A , and wavelength, λ) of the three tubercle geometries are given in Fig 2. The experimental data used for validation of the CFD results consisted of steady wall static pressure measurements on the top and bottom meridian of the ducts, and steady total pressure measurements at the duct exits. 3D effects such as swirl and the topology of separated regions can not be investigated using the experimental data, leading to a need for CFD flow fields to enable the flow mechanisms behind the experimental results to be investigated. The CFD flow fields can be used to complement the existing design philosophy, allowing for more informed decisions to be made when improving the tubercles.

The function of an S-duct diffuser is to redirect flow from the outside of the fuselage of an air vehicle and decelerate it before the fan face of an embedded engine². An engine face Mach number of 0.4-0.6 is usually targeted³. S-ducts are often used in unmanned aerial vehicles (UAVs), older transport aircraft, combat aircraft, cruise missiles^{3,4}, and boundary layer ingesting propulsion on blended wing/body designs⁵. To avoid a degradation in compressor surge margin and propulsion system efficiency, an ideal S-duct would provide a uniform axial velocity and pressure distribution at the engine face², but the behaviour of the boundary layer in the hostile environment of an adverse pressure gradient and duct

1
2
3 curvature causes secondary flows and separations which complicate intake development.
4 Due to this, large S-duct curvatures are avoided where possible⁶.
5

6 However, there are many motivations for the use of high offset/curvature S-ducts. The first
7 of these is space constraints and weight savings. For instance the McDonnell Douglas F/A-
8 18 Hornet is a small aircraft, it thus requires short, highly curved S-ducts to route the air
9 from outside the fuselage to its twin embedded engines². Current UAVs are another case in
10 point, as the length of the propulsion system is currently dictating the overall size of the
11 aircraft⁶. High curvature ducts are also useful for the reduction of an aircraft's Radar Cross
12 Section (RCS) - low RCS intake design necessitates 100% line-of-sight blockage of the
13 engine fan rotor⁷. Examples of this on combat aircraft are the Lockheed-Martin F-22 Raptor
14 and F-35 Lightning II. Due to the advantages of high offset S-ducts, there is considerable
15 interest in using flow control devices to control the secondary flows and separation within
16 the duct, alleviating the negative effects of the adverse pressure gradient and duct
17 curvature.
18
19
20
21

22 S-duct flows

23 Intrinsic S-duct flow regime

24
25 The intrinsic flow mechanism in S-duct diffusers is well known, and often given in
26 textbooks on internal flow and intake aerodynamics. In the first bend, the centrifugal
27 pressure gradient is proportional to $\rho U^2/R$, where U is the free stream velocity, ρ is the
28 fluid density, and R is the duct radius of curvature. Considering now the low-momentum
29 fluid in the boundary layer, moving with velocity $U' < U$, the local pressure gradient $\rho U'^2/R$
30 is too small to balance the pressure difference between the inside and outside of the bend,
31 leading to the boundary layer fluid migrating to the inside of the bend, and the high velocity
32 core migrating to the outside⁸. If the boundary layer at the inlet is symmetrical, the flow
33 will return to the outside of the bend across the middle of the duct⁹, rolling up into two
34 discrete contra-rotating vortical structures called Dean vortices¹⁰.
35
36
37
38
39

40 In the second bend, the centrifugal pressure gradient is reversed in direction, and the low
41 momentum fluid (inside of the first bend), where it is not in a position to be driven back
42 circumferentially - it thus persists to the engine face face⁹. Viscous effects provide the initial
43 low momentum fluid that causes the secondary flow, but the generation and downstream
44 evolution of the vortices is predominantly an inviscid effect¹⁰. In diffusers with sharp
45 bends, wall static pressure measurements have implied the existence of a separated region
46 caused by the interaction of the adverse pressure gradient and migrated low-momentum
47 fluid existed downstream of the first bend. This was confirmed by laser doppler
48 anemometry measurements performed by Whitelaw and Yu⁸. Due to the presence of
49 several interacting flow mechanisms, turbulent S-duct flows are very challenging to predict
50 accurately¹¹.
51
52
53
54
55
56
57
58
59
60

S-duct performance

Widely used reduced order metrics for quantitatively assessing the three aspects of S-duct steady state performance are outlined below, definitions are given in the appendix. The coefficients are considered on the Aerodynamic Interface Plane (AIP), the location of which is generally agreed upon by engine and airframe manufacturers.

Total pressure loss:

High values of total pressure loss within the intake lead to a reduction in the overall efficiency of the propulsion system¹², and are also often symptomatic of issues with total pressure distortion and swirl. It is measured by the average total pressure loss coefficient,

$$\gamma_{avg} = 1 - (p_{02}/p_{01}) = 1 - \pi_{avg}$$

where p_{02} and p_{01} are the average total pressure on the AIP and inlet, and π_{avg} is the average total pressure ratio.

Swirl:

The second consideration is swirl, the non-axial component of the flow on the engine face. It is caused by secondary flows within the duct, particularly those set up by the first bend⁹. In experiments by Meyer et al.¹³, twin vortices generated by a delta wing placed in front of the compressor face were found to reduce surge margin by 26%, and compressor efficiency by 7% due to changing the nominal incidence angle of the flow on the first compressor (or fan) stage from design conditions¹⁴. It is measured by the maximum swirl angle, α_{max} , the worst 60° sector distortion coefficient, SC(60), and the average swirl intensity, SI_{avg} ¹⁴.

Total pressure distortion:

The third aspect is distortions in the total pressure field at the engine face. These are caused by secondary flows and separations within the S-duct. They can lead to fan and compressor blade fatigue, and reduce the surge margin of the compressor¹². The descriptors used in papers by Asghar et al.^{1,3,15,16} are used here for the sake of easy comparison with experimental data. For all the distortion coefficients discussed in this report, a high value corresponds to a more severely distorted AIP. A simple metric is the worst 60° sector distortion coefficient, DC(60)⁹. More complex coefficients include the circumferential distortion coefficient, $(\Delta PC/P)_{avg}$, and the radial distortion coefficient, $(\Delta PR/P)_{max}$ ^{3,9,15}.

Vortex generators and boundary layer fences

Typical vortex generators (VGs) are a passive flow control (PFC) method that take the form of either vanes or ramps, with their tips located just outside of the boundary layer to allow for the greatest interaction between low momentum fluid in the boundary layer and the stream-wise vortices generated by the VGs. The vortices are highly effective in adverse pressure gradients and strong secondary flows. They work by entraining high momentum

1
2
3 fluid into the boundary layer, and thus delaying separation⁶. The potential gains with the
4 application of VGs are shown in many papers. Allan et al.¹⁷ found that they can reduce
5 $(\Delta PC/P)_{avg}$ by 80%, and decrease DC(60) from 64% to 3.5% in a boundary layer ingesting
6 inlet. Tanguy et al.¹⁸ achieved a 50% reduction in SI_{avg} and DC(60) and a 30% decrease in
7 γ_{avg} , although there was some local increase in α . They also found that there was a strong
8 dependence between VG performance and VG height. Tournier⁴ observed that VGs are most
9 effective when orientated to produce co-rotating vortices that oppose near-wall secondary
10 flows. The disadvantage of using VGs is that they are a source of parasitic drag, and are
11 vulnerable to damage from foreign object digestion^{6,19}.
12
13

14
15 Boundary layer fences and fins also reduce the intensity of secondary flows by blocking or
16 redirecting the low momentum fluid in the near wall region¹⁹. Parham et al.⁵ were able to
17 lower DC(60) by 11% with these PFC measures, but also found that they increased γ_{avg} by
18 52%. Results for a duct with an asymmetric boundary layer (and resulting bulk swirl)
19 presented by Seddon report a reduction in SC(60) of almost 100%, provided that the fence
20 is situated where crossflow velocities are high⁹.
21
22

23 Experimental method and tubercle background

24
25 A schematic of the RMC duct with the location of the nominal inlet plane and the AIP is
26 shown in Fig. 3. The ducts in this report are considered in their belly-mounted orientation,
27 with the inlet below the AIP. The AIP diameter, D is 0.1016 m, which along with a Mach
28 number of 0.8 on the nominal inlet plane, gives a Reynolds number of 1.4×10^6 . The aspect
29 ratio of the duct (W/H) is 1.49, and the area ratio between the inlet plane and AIP is 1.57.
30 The duct offset (vertical distance from the centre of the inlet to the centre of the AIP) is
31 1.31D. Steady experimental data from the RMC Transient Transonic Wind-tunnel is
32 available for wall static pressure taps on the top and bottom meridian of the duct, and total
33 pressure probes from a 5-probe rotating rake on the AIP. The Transient Transonic Wind-
34 tunnel is an indraft tunnel; ambient air is drawn through the bell mouth and duct, the outlet
35 of which is connected to a valve and vacuum tank. The reader is referred to Asghar et al.³
36 for more detail on the experimental methodology.
37
38
39
40
41
42
43
44
45
46
47
48
49
50
51
52
53
54
55
56
57
58
59
60



Figure 3. Duct dimensions and nominal inlet and AIP locations.

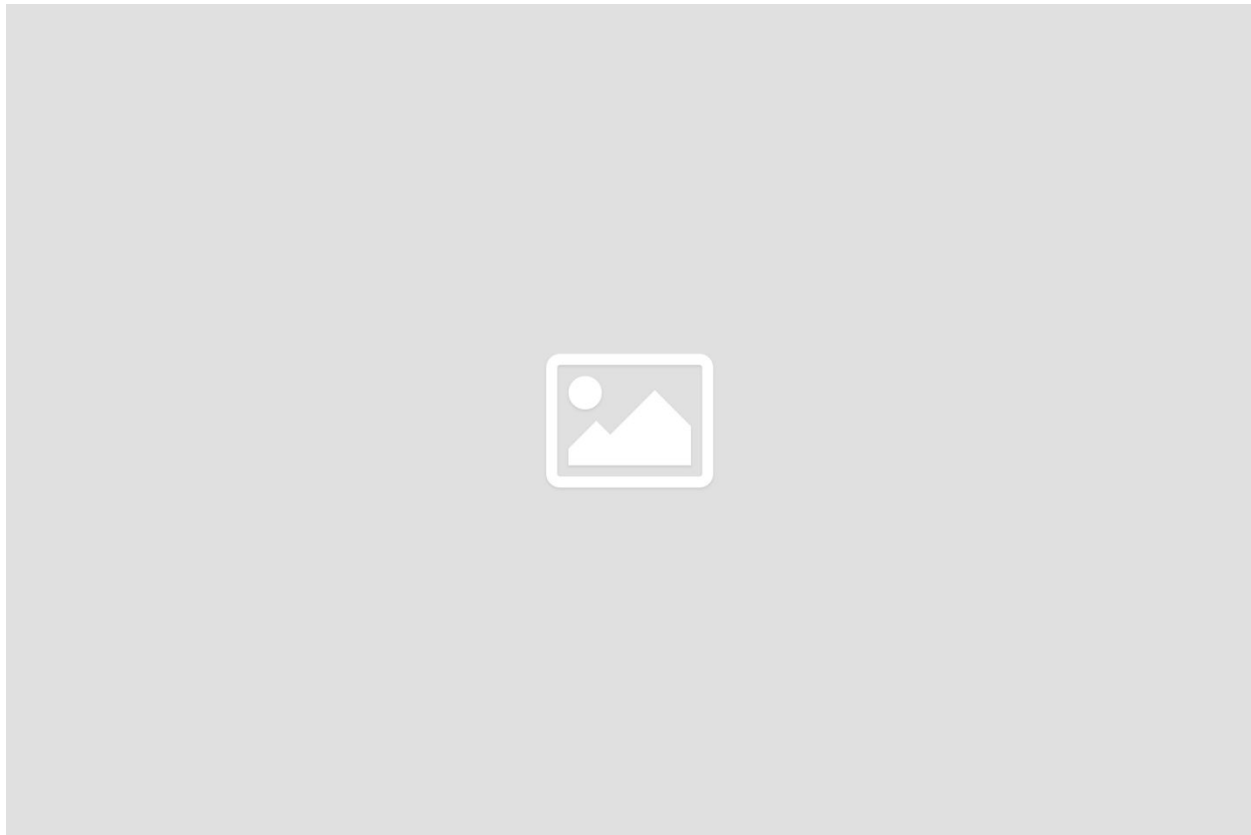
Tubercles are a novel bio-inspired PFC method that work by generating counter rotating vortices that re-energise the boundary layer in a similar manner to VGs, delaying separation. They have been demonstrated successfully in external flow on the suction surfaces of wings, hydrofoils, and wind turbine blades²⁰. As well as a baseline duct with no tubercles, three ducts with different tubercle geometries were simulated - these are denoted by FC1, FC2, and FC3 (see Fig. 1). The tubercles in FC1 and FC2 have sinusoidal cross sections. FC1 has a larger amplitude and wavelength, and FC2 is stream-wise longer. FC3 has the same stream-wise length as FC2, but has shallower valleys. During experiments, FC1 was found to give earlier separation, this was hypothesised to be because the deep valleys were concentrating low-momentum fluid, leading to the shallower tubercle amplitude in FC2. FC3 extends this principle further, leading to a sinusoidal tubercle profile being abandoned. For full details of the tubercle geometries, see Asghar et al¹.

CFD methodology

Boundary conditions

The boundary conditions used in the computations are shown in Fig. 4. The results were insensitive to the assumed turbulence intensity (TI) and viscosity ratio (TVR) at the

1
2
3 domain inlet. This was because the domain inlet turbulence had decayed significantly by
4 the time it was convected to the duct inlet, leading to turbulent production from the duct
5 walls being the dominant source of turbulence within the duct. Total pressure sweeps were
6 conducted on the pressure outlet to give an area averaged Mach number of 0.8 on the
7 nominal inlet plane. Total pressures of around 0.825 bar were found to be a good starting
8 point; generally only two or three sweeps were needed before the required Mach number
9 was reached. The duct is symmetrical about the XZ-plane, so only half the duct was meshed
10 to reduce computational requirements.
11
12



13
14
15
16
17
18
19
20
21
22
23
24
25
26
27
28
29
30
31
32
33
34
35
36
37
38
39
40 *Figure 4. Simulation boundary conditions.*

41 42 Mesh

43
44 Pointwise v18 was used to generate the meshes. An example mesh is shown in Fig. 5 for
45 duct FC3, which was the most challenging duct to mesh due to the high curvature on the
46 tubercle peaks. The domain volume was filled using an 8-10 million cell hybrid mesh with a
47 50 or 64 cell thick hexahedral boundary layer, with the wall adjacent cell height set to 0.8μ
48 m to give a y^+ of less than 1. The 64 cell boundary layer (and 10 million cell mesh) was
49 used with the FC ducts to better resolve the flow downstream of the tubercles. The smooth
50 change in cell size between the hexahedral and tetrahedral zones of the hybrid mesh is
51 shown on the symmetry plane in Detail A, Fig. 5. The surface mesh was clustered
52 circumferentially towards the top and bottom meridians, primarily to provide sufficient
53
54
55
56
57
58
59
60

1
2
3 geometric resolution to smoothly resolve the tubercles, although it also improved the
4 resolution of the generated flow features.
5



33 *Figure 5. FC3 mesh.*

34
35 The pressure inlet had a radius of $3D$, which was found by computations on similar ducts
36 by Asghar et al.³ to be sufficiently large to not affect the solution. Similarly, the duct outlet
37 was extruded for a further $1D$ down stream to avoid interactions with the pressure outlet
38 boundary condition affecting the AIP. Extending this to $3D$ was found to make no difference
39 to the results. The transition between the hybrid mesh and the prism extrusion is shown in
40 Detail B, Fig. 5.
41

42
43 The mesh used was finer than meshes used by Asghar et al.^{3,15}, which have been shown to
44 give mesh independent solutions on similar transonic S-ducts. Using a coarser tetrahedral
45 mesh was found to give the same solution, but made little difference in solution time due to
46 convergence issues associated with the pyramid cells used to transition between the
47 structured boundary layer mesh and the tetrahedral cells in the unstructured mesh.
48 Computations on an fully hexahedral OH-grid mesh for FC1 gave near identical simulated
49 flow fields, so the extra meshing time required was not justified for the other ducts. All
50 results presented in this paper use hybrid meshes.
51
52
53
54
55
56
57
58
59
60

Solver settings

The Reynolds-Averaged Navier-Stokes (RANS) equations were solved using the pressure based solver in ANSYS Fluent 15.0. Pressure-velocity coupling was done using the SIMPLE algorithm. Default under relaxation factors were used for all solver variables except energy, this was reduced from 1 to 0.95 to prevent the temperature from diverging in the first few iterations. Second order upwind discretisation was used for all variables in the final solution, the first 2000 iterations were run with the first order upwind discretisation on the turbulent flow variables to aid solution stability. Good convergence (scaled residuals $< 5 \times 10^{-5}$ for continuity, and $< 1 \times 10^{-5}$ for all other variables) was achieved for all simulations. An ideal gas model for air was used, and the effects of viscous heating were included.

Results - RANS modelling investigation

Computations were carried out using two different RANS turbulence models: Menter's hybrid SST Linear Eddy Viscosity Model (LEVM)²¹, and the realisable k- ϵ LEVM of Shih et al.²² The simulations were then validated against the experimental data of Asghar et al.¹ Duct FC1 was used as a representative environment for transonic S-ducts with passive flow control.

Shear Stress Transport (SST) model

The SST LEVM uses the Wilcox k- ω (WKW) model near walls, and the standard k- ϵ (SKE) model elsewhere²¹. The SST model attempts to model some of the effects of Reynolds' stress anisotropy within the form of an LEVM by using Bradshaw's assumption that the Reynolds' shear stress in a boundary layer is proportional to the turbulent kinetic energy k , according to $-\overline{u'v'} = \rho a_1 k$ with the constant $a_1 \approx 0.31$ ²³. It is not desirable to use this equation away from walls, so the turbulent viscosity is calculated as

$$\mu_t = \frac{\rho a_1 k}{\max(a_1 \omega, S F_2)}$$

where F_2 is a blending function that equals one from the wall through to past the wake region of the boundary layer and zero in the free-stream, and S is the strain rate magnitude²¹. In this way, the model effectively limits the turbulent shear stress in the boundary layer and adverse pressure gradient regions.

The wall static pressure coefficient is defined as

$$C_p = \frac{p_w - p_1}{p_{01} - p_1}$$

where p_w is the wall pressure, and p_1 is the average static pressure on the inlet plane. The C_p distribution predicted by the SST model and the Spalart-Shur curvature correction term²⁴ is shown in Fig. 6 (SST31). The large flat regions between $x/D = 0.5$ and $x/D = 1.5$ on

1
2
3 the top meridian and after $x/D = 2.2$ on the bottom meridian indicate large regions of flow
4 separation, which occurs earlier and recovers more slowly than indicated by the
5 experimental data. The large decrease in C_p after $x/D = 2.5$ on the top meridian is due to the
6 substantial flow blockage caused by the separated region on the bottom meridian
7 accelerating the flow and reducing the static pressure. A similar effect from the over-
8 prediction of separation on the top meridian is seen in the minima at $x/D = 1.9$ on the
9 bottom meridian. The over-prediction of separation leads to an over-prediction of total
10 pressure losses; the computation gives $\gamma_{avg} = 0.138$, which exceeds the experimental value
11 of 0.062 by 122%.
12
13
14
15
16
17
18
19
20
21
22
23
24
25
26
27
28
29
30
31
32
33
34
35
36
37
38
39
40



41
42 *Figure 6. Static pressure distributions for duct FC1. SST31 indicates that $\alpha_1=0.31$. Markers*
43 *are experimental values from Asghar et al.¹ Solid lines/squares: top meridian. Dot-dashed*
44 *lines/triangles: bottom meridian. Tubercle positions marked in grey.*
45

46 **The effect of SST stress limiting**

47

48 The effect of the shear stress limiter is to reduce mixing of high-momentum free-stream
49 fluid into the near-wall layer by turbulent diffusion, giving the model excellent
50 performance for many canonical 2D flows²¹. However, the excessive strength of the stress
51 limiter in thick boundary layers and recirculating regions has been shown to cause an over-
52 prediction of separation in flows such as asymmetric diffusers²⁵, transonic
53 shockwave/turbulent boundary layer interactions^{26,27}, and wing-body junctions²⁸.
54
55
56
57
58
59
60

The value of a_1 was increased in 0.03 increments up to 0.40. The potential need for adjustments of this kind was noted when the model was introduced by Menter²¹. With reference to Fig. 6 (SST34 and SST37), it can be seen that this markedly improves the behaviour of the SST model. The onset of separation is now predicted more accurately, with $a_1 = 0.37$ matching experimental onset of separation almost exactly on the bottom meridian, although recovery is still delayed. On the top meridian, separation is still predicted early, but the wall static pressure recovers to almost match the experimental data until the effect of the blockage caused by the delayed recovery on the bottom meridian bend becomes significant after $x/D = 2.5$. The effects of the tubercles on the first bend are not resolved, as they lie within the excessively large computed separated region.

Diminishing returns from further increasing a_1 are evident in the values of γ_{avg} , which decreases rapidly initially, with $\gamma_{avg} = 0.133$ for $a_1 = 0.34$, but then stabilises when $a_1 = 0.37$ and 0.40 , which both give $\gamma_{avg} = 0.110$. This has also been observed by Georgiadis and Yoder²⁷, where increasing a_1 beyond 0.37 had no effect, as the stress limiter was no longer reached. Therefore, stress limiting is not wholly responsible for the unsatisfactory results.

Further investigation found that the inclusion of the curvature correction negatively affected results. Although one would expect the curvature correction to improve the results around the tubercles, it causes the separated regions of the flow to increase in axial extent due to the suppression of turbulent production in regions of convex curvature on the inside of the bends^{23,24}. When the curvature correction was removed, γ_{avg} improved from 0.110 to 0.105 with $a_1 = 0.37$. Laminar-turbulent boundary layer transition modelling did not change results, as transition occurs very early on within the duct. Further improvements (at the cost of decreased generality) could be made by calibration of the coefficients in the dissipation rate equation of the SST model in WKW mode - the standard values lead the model to predict a low μ_t , sensitising the SST model further to adverse pressure gradients, even when the stress limiter is not reached²⁵.

Realisable k- ϵ (RKE) model

The RKE LEVM model proposed by Shih et al.²² has two key differences to the SKE model: a stress limiter and an alternative formulation for the ϵ equation (based on the mean square vorticity fluctuation), which is a large source of error in the SKE model, particularly in separated, highly strained, or rotating flows²². A realisable model is one that will only predict physically tenable Reynolds stress fields. There are two conditions for realisability to be satisfied, positivity of normal Reynolds stresses, and the Schwarz inequality:

$$\left\{ \frac{\overline{u'v'^2}}{\overline{u'^2} \overline{v'^2}}, \frac{\overline{v'w'^2}}{\overline{v'^2} \overline{w'^2}}, \frac{\overline{u'w'^2}}{\overline{u'^2} \overline{w'^2}} \right\} < 1.$$

It is well known that the SKE model breaks these constraints in the case of large mean strain rate²². The stress limiter in the RKE model is formulated specifically to maintain

realisability, and takes the form of a variable C_μ in the turbulent viscosity equation $\mu_t = \rho C_\mu k^2/\varepsilon$ from the SKE model. In a non-rotating frame of reference, C_μ is given by

$$C_\mu = \frac{1}{A_0 + A_s U^{(*)} k/\varepsilon}$$

where A_0 is a constant, $U^{(*)} = \sqrt{S_{ij}S_{ij} + \Omega_{ij}\Omega_{ij}}$, S_{ij} is the rate-of-strain tensor, and Ω_{ij} is the vorticity tensor. A_s is a fairly complex function of the third invariant of the rate-of-strain tensor, $S_{ij}S_{jk}S_{ki}$ ²³.

Liou et al.²⁶ found that the model out performs the SST model in terms of mean-velocity profile and static pressure distribution for transonic bump flow, a test case that is held up as particularly suitable for assessing the performance of turbulence models in transonic separated flows. An additional advantage of the RKE model is that its stress limiter and response to curvature is very general, and derived from rigorous formalism, as opposed to ad-hoc empirical corrections as in the SST model²³.

Fig. 6 shows that the RKE model performs much better than the SST model for FC1. Excellent agreement with experimental static pressure data is achieved on the top meridian, and on the bottom meridian, the only discrepancy between the computation and experiment is the slightly late onset of separation at $x/D = 2.2$, which causes an elevated static pressure in the separated region due to the diffusion in the duct. Despite this, losses are predicted well, giving a γ_{avg} of 0.064, which is 3% above the measured value.

The dominant reason for the difference in the quality of predictions is the stress limiter of the SST and RKE models. For instance, when a_1 in the SST model was set to 0.31, the maximum value of μ_t in the domain was 0.0848 Pa · s, which is much lower than the maximum value of 0.298 Pa · s computed by the RKE model. As a higher μ_t stabilises the boundary layer, the effect of the severity of the SST stress limiter becomes clear.

The results in this section illustrate that the RKE model is clearly the best model considered - it gives the most accurate results, and does not need stress limiters and other coefficients to be calibrated to match the experimental results. As a result of this, the RKE model has been used for all further computations in this paper.

Results - static pressure distributions

The distribution of C_p on the top and bottom meridian is plotted in Fig. 7 for the remaining three ducts. The typical behaviour described by Whitelaw and Yu⁸ is observed here; after a small region of constant velocity, the top meridian shows a rapid acceleration, corresponding to a decrease in the static pressure, followed by diffusion through the rest of the duct. The bottom meridian exhibits a region of deceleration in the first bend, followed by an acceleration in the second bend¹. The initial sharp decrease in static pressure at $x/D = 0.25$ on the top meridian has been observed for other ducts with high subsonic inlet velocities by, for example, Asghar et al.^{3,15}, and Tournier⁴. Tournier found that this was due

1
2
3 to the flow in the inlet becoming choked after the bell mouth. In the RMC ducts it is a local
4 effect, as only the flow on the top meridian is accelerated by the duct curvature.
5
6
7
8
9
10
11
12
13
14
15
16
17
18
19
20
21
22
23
24
25
26
27
28
29
30
31
32



33 *Figure 7. Static pressure distributions on the top and bottom meridians. Markers are*
34 *experimental values from Asghar et al.¹*
35

36 **Baseline duct:**

37
38 Fig. 7a shows the static pressure distribution for the baseline. This computation achieved
39 the poorest agreement with experimental data, this is seen in three key areas. First, the
40 flow acceleration on the top meridian occurs early, and the flow begins to diffuse earlier,
41 leading to an elevated static pressure on the top meridian down-stream (compared to
42 experimental data). Second is that recovery is predicted too soon after the first bend -
43 separation is evident in the inflexion in the experimental static pressure between $x/D = 0.9$
44 and 1.5 on the top meridian - the computation predicts the axial position of the onset of
45 separation well (although it overestimates the static pressure), but recovers by $x/D = 1.1$.
46 This leads to even more excessive diffusion, and an over estimation of C_p at the AIP. The
47 third feature is the late onset of separation and very rapid recovery after the second bend
48 around $x/D = 2.8$ on the bottom meridian. Experimental data indicates that this should
49 occur between $x/D = 2.5$ and 2.8 . There are implications for the accuracy of results
50 presented later in this paper, as the wake from the separation is the dominant feature on
51 the bottom half of the total pressure distribution on the AIP, and the top-bottom pressure
52 differential is the driver for the swirl flows.
53
54
55
56
57
58
59
60

Duct FC1:

In Fig. 6 (RKE), it can be seen that the static pressure distribution for FC1 is similar to that of the baseline duct, although the experimental data shows that the tubercles have achieved more rapid recovery and more gradual diffusion through the first bend, and earlier separation and recovery after the second bend¹. This improvement in S-duct performance is not reflected in the computational results due to the extent of the separated region being under-predicted in the baseline simulation. The earlier occurrence of separation on the second bend compared to the baseline is due to the collection of low momentum fluid in the large valleys between tubercles; this effect is mentioned briefly by Asghar et al.¹ and is investigated further later.

Duct FC2:

The distribution shown in Fig. 7b shows an improvement over both the baseline and FC1. The separated region on the first bend extends from $x/D = 1.05$ to 1.2 (compared to 0.9 to 1.5 on the baseline duct). On the second bend, the separated region has been eliminated almost entirely in the experimental data, although there is a large difference between the top and bottom meridian, indicating poor flow uniformity on the AIP¹. The elimination of the second separated region is not observed in the computational results; a separation region similar to duct FC1 is observed in these. Recovery after the second bend is predicted well, although the wake from the separated region will affect the accuracy of the AIP total pressure distribution.

Duct FC3:

Referring to the experimental data in Fig. 7c, it can be seen that FC3 performs in very similar manner to FC2, with the only major advantage being the smaller difference between the top and bottom meridians at the AIP¹. The accuracy of the computational results is similar to the baseline although better general agreement is achieved; the static pressure is slightly over-predicted after both bends.

The reason for the poor predictions in the baseline duct in comparison to the other ducts is the effect of the valleys. In the FC ducts, the valleys rapidly concentrate low-momentum fluid, triggering separation. As this is a geometric effect that is present in the experimental data the computational separation still occurs in roughly the correct place in these ducts. In comparison, in the baseline duct, there are no valleys, meaning that the onset of separation is solely governed by the effects of the turbulence modelling.

Results - swirl

Although no experimental data is available for this variable, swirl is discussed here, as aside from its importance from an engine integration standpoint, it is the secondary flows that manifest themselves as swirl on the AIP that cause much of the total pressure distortion. The distribution of the swirl angle, α is shown in Fig. 8, and swirl metrics are shown in Table 1.

Table 1. Computed and experimental S-duct performance metrics. Experimental values from Asghar et al.¹

The swirl distributions in Fig. 8 qualitatively match what one would expect from the intrinsic S-duct flow regime discussed earlier⁸⁻¹⁰. Comparison with Particle Image Velocimetry (PIV) studies²⁹ and turbulence-resolving simulations^{14,30} on other S-ducts show a similar flow structure on the AIP, and similar values of coefficients, giving confidence that these results are in the correct neighbourhood.

Considering the right hand side of the plots, in the sector between the 12 o'clock and 2 o'clock positions, the Dean vortices that have persisted from the first bend are visible, with the flow towards the top meridian causing the maxima in α at the 1 o'clock position, then returning down the duct centreline, and then migrating outwards towards the duct walls. Also visible is some flow being driven towards the bottom meridian in the sector between the 3 o'clock and 6 o'clock positions. The baseline, FC2, and FC3 have these features directly adjacent to flow residual from the first bend returning to the top meridian; a long narrow vortex occurs in this region.

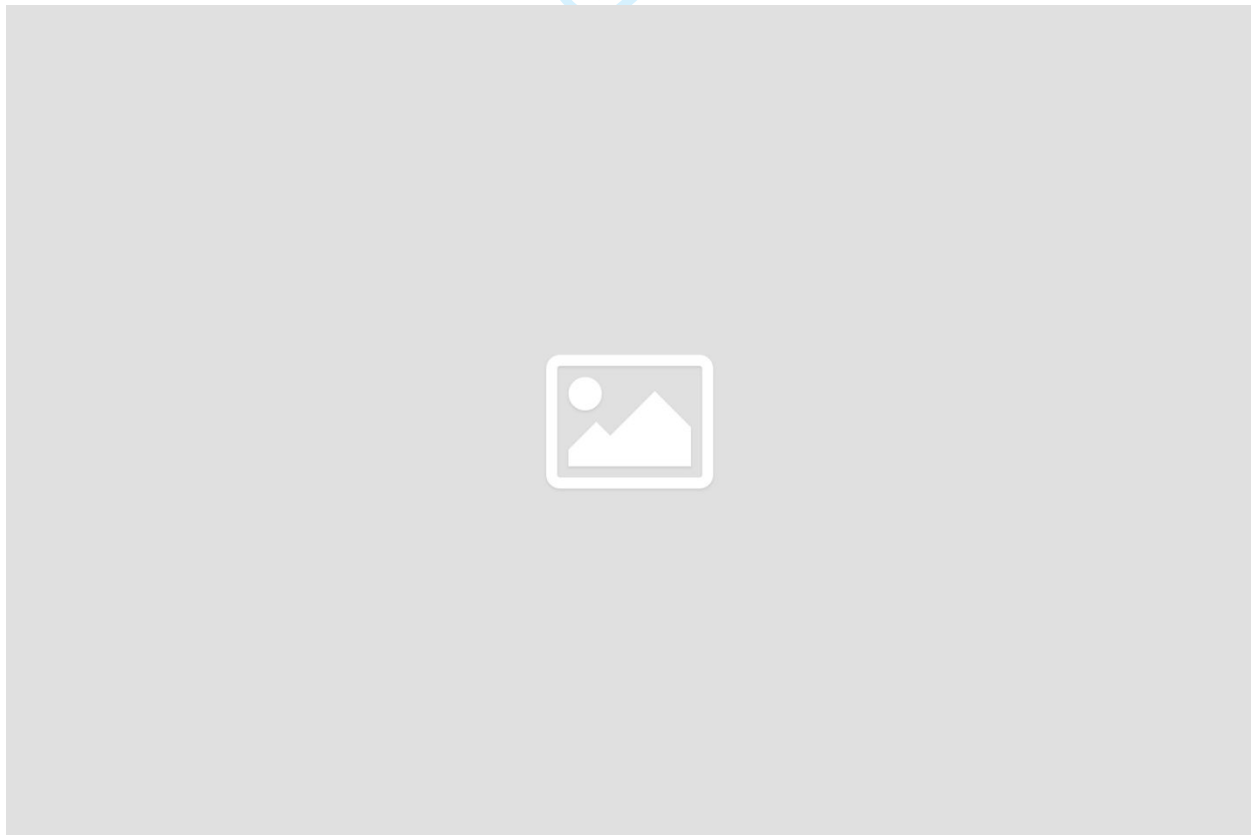


Figure 8. AIP swirl angle as viewed from downstream. Anticlockwise flow is positive.

The values of α_{max} and SC(60) are both governed by the magnitude of the maxima in the swirl at the 1 o'clock position noted above, although the negative swirl region where the Dean flow is returning to the duct wall offsets this slightly in the SC(60) coefficient. The baseline duct is predicted to perform the best in this regard by the simulation, and FC2 the worst. SI_{avg} considers the entire AIP, not just localised areas, hence it does not follow the same trend as the other two coefficients. In particular, FC1 has a lower average swirl intensity than FC3. This is due to the bottom half of the AIP of FC1 exhibiting very little swirl, whereas in FC3 this region is dominated by flow residual from the first bend heading to the top meridian (see Fig. 8b,d). The larger profile of the tubercles on the first bend in FC1 seems to suppress the formation of Dean vortices, leading to a reduced SI_{avg} .

It is likely that the computations have under-predicted the swirl velocities for the baseline and to a lesser extent, FC3. In the first bend in these ducts, the difference in static pressure between the top and bottom meridian has been under-predicted by the CFD (Figs. 6,7). It is this pressure differential that is responsible for the formation of the Dean vortices, the dominant feature of the swirl distributions on the AIP, so its under-prediction implies that the swirl has also been under-predicted.

Results - total pressure distortion and losses

Total pressure ratio distribution

The computational and experimental distribution of the total pressure ratio, $\pi = p_0/p_{01}$, on the AIP is shown in Fig. 9 for all four ducts. The plots all show the same three distinct regions: a medium total pressure region ($0.85 < \pi < 0.90$) around the top meridian, a high total pressure region ($\pi > 0.96$) that spreads laterally across the entire AIP at its vertical centre, and a low pressure region ($\pi < 0.82$) at the bottom meridian. The geometry and severity of the three regions varies considerably depending on the duct, so they are discussed on a region-by-region basis below:

Medium total pressure region:

This region consists of a central stem at the top meridian, and two lobes, which are indicative of the Dean vortices. The total pressure ratio is low in this region because the Dean vortices, aside from generating internal losses through viscous dissipation, entrain low energy fluid from the boundary layer and the edge of first separated region. The ducts are split into two groups here: baseline and FC3, and FC1 and FC2. The total pressure in this region is higher in the latter group, this is due to the more severe maximum swirl (up to 42% of the average axial velocity for FC2) leading to a higher velocity magnitude, and thus a higher total pressure.



Figure 9. AIP total pressure ratio. Top: computational results. Bottom: experimental results from Asghar et al.¹

The exact location of the Dean vortices is not visible in the experimental data, and the total pressure in their cores is higher than in computations, particularly for the baseline and FC3. For example, the computations on FC3 found $\pi = 0.84$ in the Dean vortex cores, whereas the experimental data gives $\pi \approx 0.89$. This might indicate some degree of unsteadiness in the Dean vortices' position that was not captured in the simulation - if they were to move around, the time averaged total pressure of this location would be increased by higher total pressure regions moving over it.

Low total pressure region:

The separated region from the second bend (and its associated reversed flow and high losses) extends beyond the AIP for all ducts. In comparison to the baseline, this region is computed to have a greater vertical extent in FC1 and FC2 - this is due to the greater stream-wise length of the separated region discussed earlier. FC2 and FC3 display small regions of low total pressure being drawn up the wall from the bottom to top meridian. This can be explained with reference to the location of the regions of high swirl returning flow to the bottom meridian in Fig. 8 - in FC1, they are much closer to the bottom meridian, and so act to oppose the lateral spread of the separated region.

The size and severity of the low pressure region is over-predicted in the simulations, and there are significant asymmetries in the experiment that are not present in the

1
2
3 computations. The asymmetries imply two things: that insufficient time-averaging was
4 conducted in the experiment (noted by Asghar et al. in previous S-duct experiments³);
5 and/or that the time-averaged effects of the unsteady flow in the separated region were
6 not captured in the simulation¹⁴.
7

8 9 **High total pressure region:**

10 Made up of effectively inviscid core flow, the shape of this region is dictated by the
11 boundaries of the two regions discussed above. The upper boundary of this region is
12 delineated much more sharply in FC1 and FC2. In these ducts, high momentum fluid is still
13 being entrained into the Dean vortices; this is visible in the "fingers" of dark red pointing
14 towards the top meridian in Figs. 9b,c. This region has a higher total pressure than
15 experimentally observed, so will compensate for the other regions when γ_{avg} is considered.
16
17

18 19 **Loss and distortion coefficients**

20
21 A better understanding of the accuracy of the simulation data can be gained by calculating
22 loss and distortion coefficients from the data in Fig. 9 for a quantitative comparison. A
23 summary of these coefficients is shown in Table 1, and the results are plotted in Fig. 10. The
24 general trend is that the CFD fails to capture the ranks of the designs, this is particularly
25 true for the distortion coefficients. The relative error (R.E.) is defined as
26
27

$$28 \quad R.E. = \frac{\phi_{comp} - \phi_{exp}}{\phi_{exp}},$$

29
30
31 where ϕ_{comp} and ϕ_{exp} are the computational and experimental values of the parameter ϕ .
32 Calculations were carried out on 5 equal area rings, split into 18 and 72 circumferential
33 points (the former was used by Asghar et al.¹) to check for dependency on the
34 measurement resolution, very little dependence was found; the results from the latter grid
35 are presented here.
36
37
38
39
40
41
42
43
44
45
46
47
48
49
50
51
52
53
54
55
56
57
58
59
60



Figure 10. Performance metric plots. (Data from Table 1.)

γ_{avg} :

This has been predicted with good accuracy for all ducts, but particularly FC1 and FC2. The largest relative error is -19% for the baseline duct, indicating an under-prediction of losses as one would expect from the discussion of Fig. 7a. In both the computation and the experiment, the highest losses are found in FC2. However, the rank of the other three ducts has not been predicted accurately by the CFD; this is primarily due to the underprediction of losses in the baseline duct and FC3. The loss coefficient is extremely sensitive - whilst the -19% error sounds large, Eqn. 1 shows that it corresponds to a relative error of +1.2% in

π_{avg} .

DC(60):

The experimental trend that the addition of tubercles decreases DC(60) was observed in all simulations except for duct FC3; where it was over-predicted by 75%. This is due to the under prediction of p_0 in the Dean vortex cores at the top meridian. DC(60) selects different sectors for the ducts (the 12 o'clock to 2 o'clock sector for the baseline and FC3, and the 4 o'clock to 6 o'clock sector for FC1 and FC2), showing that it is very sensitive to local total pressure variations. This has been noted by other authors, such as Berens et al.³¹

$(\Delta PC/P)_{avg}$:

This distortion coefficient is systematically over-estimated and fails to predict the rank of any of the designs, and is the most poorly predicted. It is dominated by the effects of the lateral extent of the low pressure region, which, as noted earlier, is over-predicted in the simulations. To check this coefficient, it was compared with the Circumferential Distortion Index (CDI) used by MacManus et al.¹⁴; an identical trend was observed.

$(\Delta PR/P)_{max}$:

This occurred in the outermost ring for all ducts. Agreement with experimental values and ranks was poor, with the radial distortion being under-predicted for FC1 and FC2 due to high total pressure in the fingers and high-velocity core, and over-predicted for the baseline and FC3 due to the low total pressure in the Dean vortex cores. To check this coefficient, it was compared with the Radial Distortion Index (RDI) used by MacManus et al.¹⁴; an identical trend was observed.

RANS methods and distortion prediction

Although the RKE turbulence closure has been found to satisfactorily reproduce static pressure distributions, the results presented in this section show that they do not give results or ranks for the total pressure distortion. Two unsteady effects dominate the dynamic behaviour of the flow inside S-ducts. The first is the unsteadiness of the separated regions downstream of both bends. The second is a related phenomenon called swirl switching, intrinsic to internal flows in curved pipes. This is where the Dean vortices alternately dominate the flow within the duct, changing the dominant swirl direction at the AIP. Proper Orthogonal Decomposition studies on PIV and Delayed Detached Eddy Simulation (DDES) data have found that the reason for the existence of this is due to the formation of instabilities in the shear layer and separated region after the first bend^{30,31}. In high-offset ducts such as the ones considered in this report, the distinction between these two mechanisms is unclear and their characteristic frequencies are broadband, although they are still present¹⁴.

Unsteady RANS (URANS) computations were carried out using the hybrid mesh of duct FC1 with time steps ranging from 2.5 μ s to 0.2 ms for a total of 40 flow through times. The peak value of π was 0.001 above the average (compared to 0.026 above the average in DDES data from MacManus et al.¹⁴), indicating no significant unsteadiness. This is due to the unsteadiness being inherently asymmetric, and thus prohibited by the presence of the symmetry boundary condition. It is unlikely that an improvement in results would have been obtained in a full duct URANS simulation - the time and length-scales of shear layer instabilities are not resolved by URANS models and the flow field lacks the clear spectral gap.

Results - mechanisms of tubercles as passive flow control

Vortex generation

The computations show that the tubercles are successful in generating stream-wise vortices, although their energising effect on the boundary layer is expected to be localised - the vortices in the key regions at the top and bottom meridian are mixed out rapidly in the separation regions after each bend. Fig. 11 shows the X-vorticity (ω_x) distribution at YZ-plane slices distributed between the reference plane and the AIP.



Figure 11. Streamlines and cross sections of X-direction vorticity for duct FC3. Inset: zoom of the bottom meridian on plane D.

Visible on the top meridian on plane A is the vorticity generated by the tubercles at the first bend transported down-stream. As separation occurs between planes A and B, these vortices have not yet been mixed out. The alternating positive and negative senses of the rotation of the vortices is consistent with counter-rotating vortices in experiments and simulations on tubercles in external flow²⁰. By plane B, the vortices in the centre of the duct have been mixed out due to the strong velocity gradients in the separated flow structure visible in the reversed streamline near the top meridian. The only vortex pair that is still visible is on the outside of the duct, avoiding the separated region. The vortex rotating in the negative sense is reinforced by the flow being driven from the bottom to the top

meridian by the duct curvature. The positive vortex is almost fully dissipated by plane C, and the negative vortex has begun to roll up into the Dean vortices.

At plane D, the vorticity generated by the second set of tubercles is seen. The discussion for this slice is similar to plane A, except for the fact that these vortices have already begun to be dissipated by other flow features in the duct, namely the separation region at the duct centre and the flow being driven towards the bottom meridian by the second bend. By the AIP, the Dean vortices and the secondary flow from the second bend dominate the vorticity distribution, although both features are altered by the tubercles.

Near-wall flow

The undesirable effect of deep valleys between tubercles was noted briefly by Asghar et al.¹ To investigate this further, skin friction lines, shown in Fig. 12 for FC2, have been used to investigate the near-wall flow. The presence of tubercles alters the flow topology at the onset of separation significantly - they deflect low momentum fluid into the valleys, thickening the boundary layer, and ultimately inducing earlier separation, as evidenced by the saddle point near the centre of the duct³². This explains the later onset of separation in FC3 compared to FC1 and FC2, as the profile of FC3 deflects less low momentum fluid into the valleys.

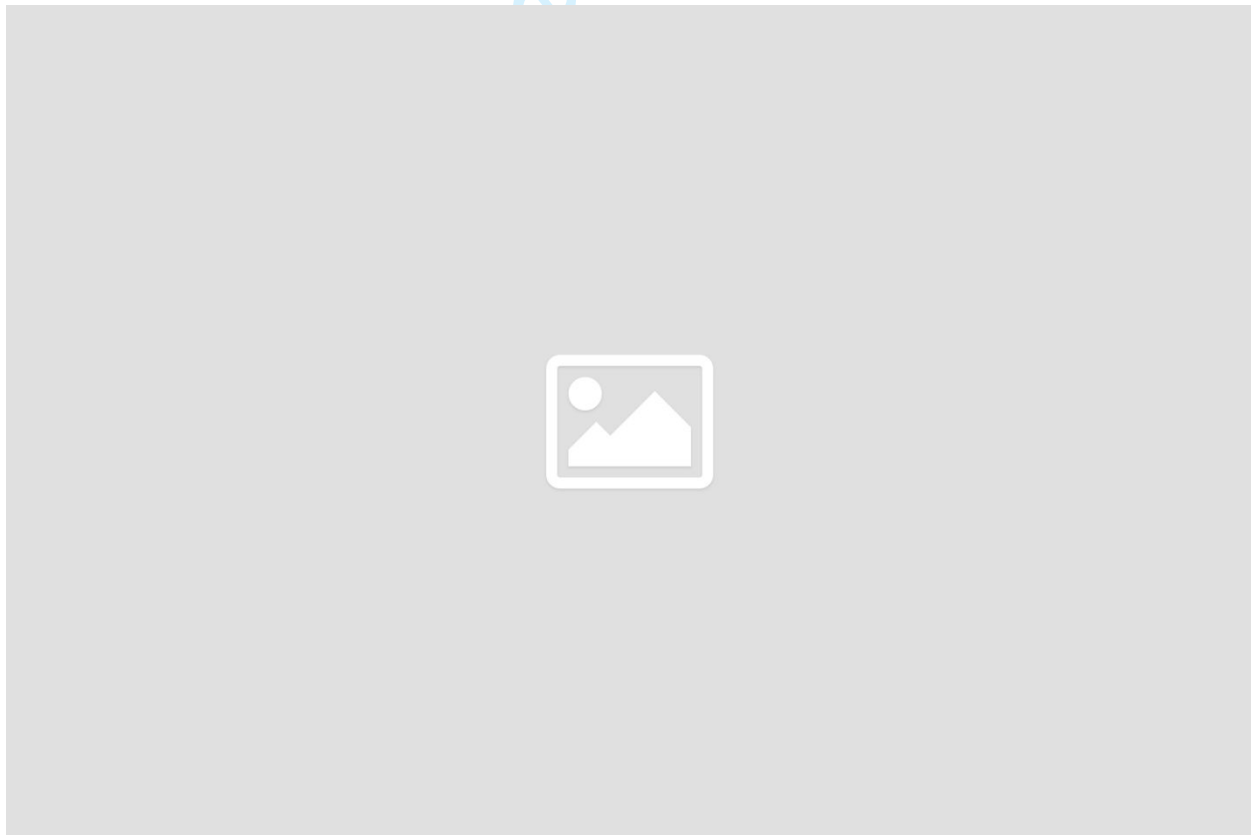


Figure 12. Skin friction lines for the top surface of the first bend for duct FC2. The blue dot indicates the saddle point, and red dashes indicate tubercle peaks. Inset: Plot location highlighted.

1
2
3 The blocking effect of the tubercle profiles in cross-flow is shown by the convergence of
4 skin friction lines at $y/D = 0.30$. This was assumed to be a negative effect in Asghar et al.¹,
5 and was a driver for the smaller amplitude of the tubercle peaks in FC2 and FC3, although it
6 is actually a similar effect to the boundary layer fences discussed by Parham⁵ and Seddon⁹.
7 This suggests that a large tubercle such as in FC1 may be desirable on the outside of the
8 duct where it will act to suppress secondary flows, but undesirable in the centre of the duct
9 where it will cause early separation. However, the tubercles are significantly stream-wise
10 shorter than the fences reported by Seddon⁹, which extend for 75% of the first bend. This
11 suggests that extending the tubercles in the stream-wise direction will improve their
12 boundary layer fence effect.
13
14
15

16 Location of losses

17
18 Contours of the local entropy generation rate, \dot{S}_{PRO} , for FC2 are shown in Fig. 13. As per
19 Kock³³, \dot{S}_{PRO} was split into viscous and heating effects, which were further split using the
20 Reynolds decomposition into their mean-flow and fluctuating flow components, the latter
21 being modelled using ε and the turbulent Prandtl number. Viscous losses from fluctuating
22 flow components were dominant, exceeding heating losses from the fluctuating flow
23 components by a factor of three, and mean-flow components by two or more orders of
24 magnitude.
25
26

27 Three loss mechanisms are visible in Fig. 13: boundary layer losses, secondary flow losses
28 from the Dean vortices, and wake losses from separated regions. The boundary layer losses
29 are fairly constant between the ducts, being dependent on mean flow velocities (but still
30 generate a lot of entropy - \dot{S}_{PRO} in these regions exceeds the scale of Fig. 13 by two orders
31 of magnitude). The secondary flow losses are due to the Dean vortices, and are visible in
32 the large regions on the top meridian at plane B. On the outside of the top of plane B is also
33 the loss core from the vortex generated by the outermost tubercle. For the baseline the
34 majority of the loss on planes A and B is in this region, before the Dean vortices track to the
35 centre of the duct downstream. This does not imply that the tubercles have reduced the
36 loss on these planes, just that they have moved the loss location. The losses within the
37 separated regions seem to be the dominant factor differentiating between the ducts.
38
39
40
41
42
43
44
45
46
47
48
49
50
51
52
53
54
55
56
57
58
59
60



Figure 13. Local entropy production rate and Mach number for duct FC2.

Conclusion

The flow within a transonic diffusing S-duct has been investigated computationally and compared to experimental data from Asghar et al.¹ Menter's SST²¹ model fails to reproduce pressure losses and wall static pressure distribution due to over-predicted separated regions caused by an over-active stress limiter. The RKE model²² fares better, but under-predicts losses for the baseline duct and FC3, and fails to give accurate results for the total pressure distortion.

Computed swirl distributions are found to reproduce those observed in S-ducts by other authors, with Dean flow from the first bend persisting to the AIP and dominating. The larger profile of FC1 in cross flow is found to act like a boundary layer fence, reducing the average swirl. The RKE model predicts static pressure distributions well, but fails to accurately predict the ranks of all the coefficients calculated to evaluate the design. Errors are particularly pronounced for the total pressure distortion coefficients, with errors up to +126%. More accurate prediction of the coefficients requires that the unsteady effects in the separation region on the first bend are captured. Despite this the CFD results have proved to be useful for qualitatively investigating the effect of the design interventions.

An improved design for the tubercles is proposed - this involves having large tubercles such as FC1 on the side to take advantage of their boundary layer fence effect, while

maintaining the use of the FC3 tubercles in the duct centre for their suppression of separation through boundary layer re-energisation.

Recommendations

Unsteady simulations are necessary to capture the intrinsic unsteadiness of the flow within S-ducts. URANS computations on half-duct geometries have shown that there is little benefit to be gained in using URANS models on the same geometry. Berens et al.³¹ have shown that little advantage can be gained with URANS or DES simulations, even on a full duct. The deficiency of DES is likely due to the models' tendency to predict early, grid-induced separation. An approach that addresses this is Delayed-DES (DDES). DDES computations in similar ducts by MacManus et al.¹⁴ predicted $(\Delta PC/P)_{avg}$ to within +23%, a marked improvement on the RANS computations in this report (between +51% and +126%).

Despite not capturing the unsteadiness and its effects on total pressure losses or distortion, the RANS simulations with the RKE model can be used as a relatively low computational cost method to drive design improvements in S-ducts with passive flow control as it allows investigations of the local flow structure over the tubercles.

Acknowledgements

The authors would like to thank William Allan, Marc LaViolette, Asad Asghar, and Satpreet Sidhu from the Royal Military College of Canada for generously sharing their experimental results and the details of the S-duct geometries. Thanks are also due to the anonymous reviewers for their help in improving this paper.

References

1. Asghar et al., "Investigation of a passive flow control device in an S-duct inlet of a propulsion system with high-subsonic flow," Proceedings of ASME Turbo Expo 2018, 2018. GT2018-76636.
2. Fiola and R. Agarwal, "Simulation of secondary and separated flow in a diffusing S-duct using four different turbulence models," Journal of Aerospace Engineering, vol. 228, no. 11, pp. 1954–1963, 2013.
3. Asghar et al., "Performance evaluation of an S-duct diffuser of a flight-vehicle inlet in high-subsonic flow," Proceedings of ASME Turbo Expo 2015, 2015. GT2015-43740.
4. S. Tournier, "Flow analysis and control in a subsonic inlet," Master's Thesis, MIT, 2005.
5. J. Parham et al., "Flow control for boundary layer ingestion in an S-duct diffuser," in 49th AIAA Aerospace Sciences Meeting, AIAA, 2011. AIAA 2011-822.

- 1
 - 2
 - 3
 - 4
 - 5
 - 6
 - 7
 - 8
 - 9
 - 10
 - 11
 - 12
 - 13
 - 14
 - 15
 - 16
 - 17
 - 18
 - 19
 - 20
 - 21
 - 22
 - 23
 - 24
 - 25
 - 26
 - 27
 - 28
 - 29
 - 30
 - 31
 - 32
 - 33
 - 34
 - 35
 - 36
 - 37
 - 38
 - 39
 - 40
 - 41
 - 42
 - 43
 - 44
 - 45
 - 46
 - 47
 - 48
 - 49
 - 50
 - 51
 - 52
 - 53
 - 54
 - 55
 - 56
 - 57
 - 58
 - 59
 - 60
6. J. Vaccaro et al., "Experimental and numerical investigation on steady blowing flow control within a compact inlet duct," *International Journal of Heat and Fluid Flow*, vol. 54, pp. 143–152, 2015.
 7. Bingaman, "Performance study for inlet installations," 1992. NASA Contractor Report 189714.
 8. J. Whitelaw and S. Yu, "Turbulent flow characteristics in an S-shaped diffusing duct," *Flow Measurement and Instrumentation*, vol. 4, no. 3, pp. 171–179, 1993.
 9. J. Seddon and E. Goldsmith, *Intake Aerodynamics*. AIAA Education Series, 1985.10.
 10. E. Greitzer et al., *Internal Flow*. Cambridge, UK: Cambridge University Press, 2004.
 11. G. Gerolymos and I. Vallet, "Reynolds-Stress Model Prediction of 3-D Duct Flows," *Flow, Turbulence, and Combustion*, no. 96, pp. 45–93, 2016.
 12. Sobester, "Tradeoffs in jet inlet design: a historical perspective," *Journal of Aircraft*, vol. 44, no. 3, pp. 705–717, 2007.
 13. W. Meyer et al., "The influence of intake swirl distortion on steady state performance of a low bypass twin-spool engine," AGARD Report, 1991. CP-498.
 14. MacManus et al., "Complex aeroengine intake ducts and dynamic distortion," *AIAA Journal*, vol. 55, no. 7, pp. 2395–2409, 2017.
 15. Asghar et al., "Entrance aspect ratio effect on S-duct inlet performance at high-subsonic flow," *Proceedings of ASME Turbo Expo 2016*, 2016. GT2016-57875.
 16. Asghar et al., "Investigation of a passive flow control device in S-duct inlet of a propulsion system with high subsonic flow," in *CASI AERO17*, 2017.
 17. Allan et al., "Optimal design of passive flow control for a boundary-layer-ingesting offset inlet using design-of-experiments," 2008. NASA/AIAA.
 18. G. Tanguy et al., "Passive flow control study in an S-duct intake using stereo particle image velocimetry," *AIAA Journal*, vol. 55, no. 6, pp. 1862–1877, 2017.
 19. L. Jenkins et al., "Flow control device evaluation for an internal flow with an adverse pressure gradient," in *40th AIAA Aerospace Sciences Meeting*, AIAA, 2002. AIAA 2002-0266.
 20. Fish et al., "The tubercles on humpback whales' flippers: application of bio-inspired technology," *Integrative and Comparative Biology*, vol. 51, no. 1, pp. 203–213, 2011.
 21. Menter, "Improved two equation $k-\omega$ turbulence models for aerodynamic flows," NASA Technical Memorandum 103975, 1992.
 22. T. Shih et al., "A new $k-\epsilon$ eddy viscosity model for high Reynolds number turbulent flows," *Computers and Fluids*, vol. 24, no. 9, pp. 229–238, 1995.

- 1
- 2
- 3
- 4 23. M. Leschziner, *Statistical Turbulence Modelling for Fluid Dynamics - Demystified*.
5 London, UK: Imperial College Press, 2016.
- 6
- 7 24. P. Smirnov and F. Menter, "Sensitization of the SST turbulence model to rotation and
8 curvature by applying the Spalart-Shur correction term," *Journal of*
9 *Turbomachinery*, vol. 131, no. 041010, 2009.
- 10
- 11 25. Apsley and M. Leschziner, "Advanced turbulence modelling of separated flow in a
12 diffuser," *Flow, Turbulence, and Combustion*, vol. 63, pp. 81–112, 1999.
- 13
- 14 26. W. Liou et al., "Turbulence model assessment for shock wave/turbulent boundary
15 layer interaction in transonic and supersonic flows," *Computers & Fluids*, vol. 29, pp.
16 275–299, 2000.
- 17
- 18 27. N. Georgiadis and D. Yoder, "Recalibration of the shear stress transport model to
19 improve calculation of shock separated flows," in *51st Aerospace Sciences Meeting*,
20 2013. NASA/TM-2013-217851.
- 21
- 22 28. Apsley and M. Leschziner, "Investigation of advanced turbulence models for the flow
23 in a generic wing-body junction," *Flow, Turbulence, and Combustion*, vol. 67, pp. 25–
24 55, 2001.
- 25
- 26 29. Gil-Prieto et al., "Convolved intake distortion measurements using stereo particle
27 image velocimetry," *AIAA Journal*, vol. 55, no. 6, pp. 1878–1892, 2017.
- 28
- 29 30. D. Gil-Prieto et al., "Delayed detached-eddy simulation and particle image
30 velocimetry of S-duct flow distortion," *AIAA Journal*, vol. 55, no. 6, pp. 1893–1908,
31 2017.
- 32
- 33 31. T. Berens et al., "Numerical simulations for high offset diffuser flows," *Tech. Rep.*
34 *NLR-TP-2014-096*, National Aerospace Laboratory NLR, 2014.
- 35
- 36 32. J. Delery, "Robert Legendre and Henri Werle: Towards the elucidation of three-
37 dimensional separation," *Annual Reviews in Fluid Mechanics*, vol. 33, pp. 129–154,
38 2001.
- 39
- 40 33. Kock and H. Herwig, "Entropy production calculation for turbulent shear flows and
41 their implementation in CFD codes," *International Journal of Heat and Fluid Flow*,
42 vol. 26, pp. 672–680, 2005.
- 43
- 44
- 45
- 46
- 47
- 48
- 49
- 50
- 51
- 52
- 53
- 54
- 55
- 56
- 57
- 58
- 59
- 60

Appendix

Performance metric definitions

Swirl

The maximum value of the swirl angle on the AIP is used as a metric for the swirl on the AIP¹⁴. The swirl angle is defined as

$$\alpha = \arctan(V_{\theta}/W_{avg})$$

where V_{θ} is the circumferential velocity on the AIP (positive anticlockwise), and W_{avg} is the average axial velocity on the AIP¹⁴. The worst 60° swirl coefficient is calculated from

$$SC(60) = \frac{V_{\theta avg 60}}{W_{avg}}$$

where $V_{\theta avg 60}$ is the average of V_{θ} in the worst 60° sector¹⁴.

The final swirl metric used in this report is the average swirl intensity,

$$SI_{avg} = \frac{1}{5} \sum_{i=1}^5 \left(\frac{1}{360} \int_{0^{\circ}}^{360^{\circ}} \alpha_i(\theta) d\theta \right)$$

where the subscript i corresponds to one of the 5 equal area rings described by the path of one the probes on the pressure rake the experimental set-up of Asghar et al.¹, as is convention¹⁴.

Total pressure distortion

$DC(\theta)$ measures the average total pressure in the worst sector of an angular extent of θ degrees ($p_{0\theta}$)⁹. It is defined as

$$DC(\theta) = \frac{p_{02} - p_{0\theta}}{p_{02} - p_2}$$

where p_2 is the average static pressure on the AIP. θ must be reasonably large; 60° is regarded as a minimum, and is also the most commonly used⁹.

The circumferential distortion coefficient is given by

$$(\Delta PC/P)_{avg} = \frac{1}{5} \sum_{i=1}^5 \left(\frac{p_{0i} - p_{0i,low}}{p_{0i}} \right)$$

where p_{0i} is the average total pressure in the i^{th} ring, and $p_{0i,low}$ is the average total pressure in all sectors of the i^{th} ring that have a total pressure lower than the ring average^{3,9,15}. The notation $DPCP_{avg}$ is sometimes used for this coefficient.

The final total pressure distortion coefficient used in this report is the radial distortion coefficient. It is defined as

$$(\Delta PR/P)_{max} = \max_{i \in [1,5]} \left(\frac{p_{02} - p_{0i}}{p_{02}} \right)$$

although it is sometimes notated as $DPRP_{max}$. The average of this coefficient across all five equal area rings is 0, so the maximum value, corresponding to the lowest average total pressure ring is used.

Nomenclature

A = tubercle amplitude

A_0 = constant in the RKE model stress limiter

A_s = function in the RKE model stress limiter

a_1 = constant in Bradshaw's assumption

C_p = wall static pressure coefficient

C_μ = constant in the turbulent viscosity equation

D = AIP diameter

$DC(60)$ = worst 60° sector distortion coefficient

F_2 = blending function in the SST model stress limiter

H = duct inlet height

k = turbulence kinetic energy

p_0 = local total pressure

p_{01} = average inlet total pressure

p_{02} = average outlet total pressure

p_1 = average inlet static pressure

p_w = wall static pressure

$R.E.$ = relative error

S = strain rate magnitude

1
2
3 S_{ij} = rate-of-strain tensor
4

5 \dot{S}_{PRO} = local entropy generation rate
6

7 $SC(60)$ = worst 60° sector swirl coefficient
8

9 SI_{avg} = average swirl intensity
10

11 u, v, w = $x, y,$ and z velocity components
12

13 u', v', w' = fluctuations of $x, y,$ and z velocity components
14

15 W = duct inlet width
16

17 x, y, z = Cartesian coordinates
18

19 y^+ = non-dimensional wall distance
20

21 α_{max} = maximum swirl angle
22

23 γ_{avg} = average total pressure loss coefficient
24

25 $(\Delta PC/P)_{avg}$ = circumferential distortion coefficient
26

27 $(\Delta PR/P)_{max}$ = radial distortion coefficient
28

29 ε = dissipation rate of k
30

31 λ = tubercle wavelength
32

33 μ_t = turbulent viscosity
34

35 π = local total pressure ratio
36

37 π_{avg} = average total pressure ratio
38

39 ρ = density
40

41 ϕ = general parameter
42

43 ϕ_{comp} = computational value of ϕ
44

45 ϕ_{exp} = experimental value of ϕ
46

47 Ω_{ij} = vorticity tensor
48

49 ω = turbulence eddy frequency
50

51 ω_x = x component of the vorticity vector
52
53
54
55
56
57
58
59
60